Experimental and Numerical Analysis of Triaxially Braided Composites Utilizing a Modified Subcell Modeling Approach

Christopher Cater and Xinran Xiao
Michigan State University, Lansing, Michigan

Robert K. Goldberg and Lee W. Kohlman
Glenn Research Center, Cleveland, Ohio

NASA STI Program . . . in Profile

Since its founding, NASA has been dedicated to the advancement of aeronautics and space science. The NASA Scientific and Technical Information (STI) Program plays a key part in helping NASA maintain this important role.

The NASA STI Program operates under the auspices of the Agency Chief Information Officer. It collects, organizes, provides for archiving, and disseminates NASA's STI. The NASA STI Program provides access to the NASA Technical Report Server—Registered (NTRS Reg) and NASA Technical Report Server— Public (NTRS) thus providing one of the largest collections of aeronautical and space science STI in the world. Results are published in both non-NASA channels and by NASA in the NASA STI Report Series, which includes the following report types:

- TECHNICAL PUBLICATION. Reports of completed research or a major significant phase of research that present the results of NASA programs and include extensive data or theoretical analysis. Includes compilations of significant scientific and technical data and information deemed to be of continuing reference value. NASA counter-part of peer-reviewed formal professional papers, but has less stringent limitations on manuscript length and extent of graphic presentations.

- TECHNICAL MEMORANDUM. Scientific and technical findings that are preliminary or of specialized interest, e.g., "quick-release" reports, working papers, and bibliographies that contain minimal annotation. Does not contain extensive analysis.

- CONTRACTOR REPORT. Scientific and technical findings by NASA-sponsored contractors and grantees.

- CONFERENCE PUBLICATION. Collected papers from scientific and technical conferences, symposia, seminars, or other meetings sponsored or co-sponsored by NASA.

- SPECIAL PUBLICATION. Scientific, technical, or historical information from NASA programs, projects, and missions, often concerned with subjects having substantial public interest.

- TECHNICAL TRANSLATION. English-language translations of foreign scientific and technical material pertinent to NASA's mission.

For more information about the NASA STI program, see the following:

- Access the NASA STI program home page at http://www.sti.nasa.gov

- E-mail your question to help@sti.nasa.gov

- Fax your question to the NASA STI Information Desk at 757-864-6500

- Telephone the NASA STI Information Desk at 757-864-9658

- Write to:
  NASA STI Program
  Mail Stop 148
  NASA Langley Research Center
  Hampton, VA 23681-2199

Experimental and Numerical Analysis of Triaxially Braided Composites Utilizing a Modified Subcell Modeling Approach

Christopher Cater and Xinran Xiao
Michigan State University, Lansing, Michigan

Robert K. Goldberg and Lee W. Kohlman
Glenn Research Center, Cleveland, Ohio

Level of Review: This material has been technically reviewed by technical management.

Experimental and Numerical Analysis of Triaxially Braided Composites Utilizing a Modified Subcell Modeling Approach

Christopher Cater and Xinran Xiao
Michigan State University
Lansing, Michigan 48910

Robert K. Goldberg and Lee W. Kohlman
National Aeronautics and Space Administration
Glenn Research Center
Cleveland, Ohio 44135

Abstract

A combined experimental and analytical approach was performed for characterizing and modeling triaxially braided composites with a modified subcell modeling strategy. Tensile coupon tests were conducted on a [0°/60°/–60°] braided composite at angles of 0°, 30°, 45°, 60° and 90° relative to the axial tow of the braid. It was found that measured coupon strength varied significantly with the angle of the applied load and each coupon direction exhibited unique final failures. The subcell modeling approach implemented into the finite element software LS-DYNA was used to simulate the various tensile coupon test angles. The modeling approach was successful in predicting both the coupon strength and reported failure mode for the 0°, 30° and 60° loading directions. The model over-predicted the strength in the 90° direction; however, the experimental results show a strong influence of free edge effects on damage initiation and failure. In the absence of these local free edge effects, the subcell modeling approach showed promise as a viable and computationally efficient analysis tool for triaxially braided composite structures. Future work will focus on validation of the approach for predicting the impact response of the braided composite against flat panel impact tests.

Introduction

Two dimensional (2D) triaxially braided composites are increasingly used in a wide variety of high-performance applications which require both the improved specific stiffness and strength of carbon fiber composites and the delamination resistance and impact toughness of a textile reinforcement architecture (Ayranci and Carey 2008). This composite reinforcement is widely used in aircraft structural components such as the fan containment system of turbine engines for which the dynamic and impact properties of the composite are crucial (Roberts et al. 2009).

These triaxially braided composites are hierarchical materials which contain several length scales. First, the macroscale refers to the overall final structure or component made with the braided composite. Second, the mesoscale refers to the length scale of the braided reinforcement architecture, whereby one models individual fiber tows. Lastly, the microscale refers to the length scale of the individual fiber and matrix components present within the fiber tow of the braid.

Traditionally, braided composite structures are analyzed the same way as laminated composite structures. In finite element analysis (FEA), the composite structures are represented by solid elements or composite shell elements with homogenized properties established by micromechanics or by material testing. In this way, the mesoscale heterogeneity of the composite is ignored.

To consider the mesoscale heterogeneity in FEA, a subcell approach has been proposed (Li et al. 2009, Blinzler 2012, Cheng and Binienda 2008, Xiao et al. 2011, Goldberg et al. 2010). The subcell approach has

several added benefits over traditional composite modeling methods. Firstly, the preservation of macroscale heterogeneity sets it apart from standard multiscale schemes, which typically define the macroscale as an orthotropic, homogeneous medium (Yuan and Fish 2008, Liu et al. 2011). These multiscale approaches are completely homogenized at the macroscopic scale, whereby no information of the local braided architecture remains. For triaxially braided composites, the braided pattern is too large to not be accounted for in the finite element analysis at the macroscopic scale. The subcell approach on the other hand provides continued heterogeneity even at the highest scale. Secondly, the semi-analytical nature of the subcell discretization allows for improved computational efficiency over complex representative unit cell (RUC) models of textile reinforced composites (Quek et al. 2004, 2006, Song et al. 2007) or the explicit mesoscale modeling of braided coupons (Zhang et al. 2013, 2014). Although these RUC models have high fidelity to capture local fiber tow interactions and matrix failures, they are prohibitively computationally expensive to scale up beyond single layer coupon tests. Both of these advantages are central to any modeling approach aiming to efficiently capture impact damage patterns shown to be dependent on the braided architecture of multi-layer triaxial braids (Roberts et al. 2009).

Although the subcell approach has been investigated by several researchers, it is still in the development stage and a comprehensive evaluation is ongoing. In this work, a combined experimental and numerical approach is undertaken to verify the efficacy of the subcell modeling approach in capturing the characteristics of a 2D triaxially braided composite. A suite of straight sided coupon tests per ASTM standards was conducted for a variety of coupon angles, including 0°, 30°, 45°, 60° and 90°. Previous work present in the current literature has only investigated the axial (0°) and transverse (90°) directions of the braided composite (Littell 2008). These results will be used to evaluate the efficacy of the computationally efficient subcell modeling approach in capturing the experimental coupon strengths and failure modes as a function of the change in coupon orientation. First, the subcell model development is outlined. Second, the characterization processes for determining material parameters of the material model within the dynamic finite element package LS-DYNA are discussed. Next, the experimental results are presented for the off-axis coupon tests. Finally, the simulation results are presented, along with modified improvements and a discussion of the presented results.

Subcell Model

Subcell Discretization

The subcell approach is outlined in Figure 1. First, the RUC is identified and partitioned into subcell regions. The four subcells shown in Figure 1 correspond to the regions where axial (0°) and braider (+60°/–60°) tows were both present (subcells A and C) and regions where only braider tows were present (subcells B and D). This partitioning follows previous subcell models (Li et al. 2009, Blinzler 2012, Cheng and Binienda 2008, Xiao et al. 2011, Goldberg et al. 2010). In this discretization, both subcells A and C had identical fiber content and differed only in the arrangements of the braider tows. The same relation is true for subcells B and D. After the establishment of subcells, the next step is to discretize the subcells using a "mosaic" approach. Thus, each subcell is approximated as a unique composite laminate which can be modeled as a laminated composite shell. By modeling each subcell as a laminated composite shell, the mesoscale heterogeneity can be preserved in the macroscale FE model.
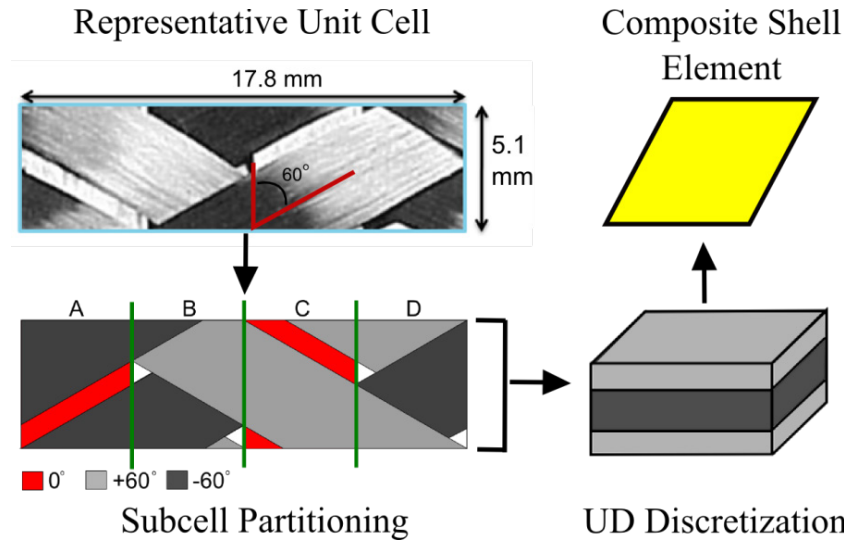
Figure 1.—Workflow of the semi-analytical subcell approach. The representative unit cell of the braided composite is partitioned into various subcells which are then discretized into a unidirectional (UD) ply approximation. The resulting subcell is modeled as a composite shell element in a finite element analysis.
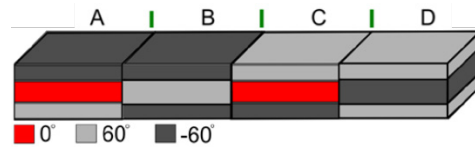

Figure 2.—The subcell UD discretization method for the absorbed matrix model (AMM) highlighting the orientation of fibers in the individual lamina layers.

A subcell may be discretized in a number of ways. Figure 2 presents a discretization using the absorbed matrix model (AMM) which was found to best capture the in-plane and out-of-plane stiffness properties of the braided composite with notable differences from other subcell approaches (Cater et al. 2014). First, in Figure 2, subcells A and C are modeled as unsymmetric laminate regions while subcells B and D are assumed to be symmetric. The asymmetry allows for the capturing of the important tension-twist coupling of the local braided regions during tensile deformations. Additionally, in the AMM it is assumed that the axial (0°) plies account for only the fiber tows, whereas the braider (±60°) plies are a homogenized representation of the braider tows and surrounding pure matrix regions. This discretization was found to best capture the local fiber volume fraction in each of the subcell regions and differs from other subcell models which modeled pure matrix regions explicitly (Xiao et al. 2011).

Determination of Unidirectional Ply Volume Fractions

The calculation of subcell laminate parameters for AMM followed the approach by Cater et al. (2014). The first step was to compute the volume of fibers in each subcell. The second step involved determining the volume fractions and respective fiber volume fractions of the unidirectional plies comprising each subcell.

The geometrical parameters of a braided composite system consisting of T700 Toray fibers with Cytec PR 520 resin, hereby referred to as PR520, are provided in Table 1. These values were used to approximate the volume of fibers in each subcell. The subcell widths W_A and W_B are measured as shown

in Figure 3, along with the subcell length, L. Figure 3 also shows the amount of braider tow (dashed yellow regions) contained within a given subcell (solid green square). It was assumed, as in Xiao (2011), that the lengths l_{bB} and l_{bA} can be used in a straight line approximation to account for all of the braider tow contained within the subcell. Figure 4 presents a three-dimensional view highlighting the determination of these braider tow lengths.

TABLE 1.—GEOMETRICAL PARAMETERS USED FOR CALCULATING
THE LAMINA THICKNESSES (T700/PR520 SYSTEM)

Label	Description	Value
W	Width of RUC (mm) [a]	8.9
W_A	Width of cell A (mm) [a]	4.201
W_B	Width of cell B (mm) [a]	4.765
h	Ply thickness (mm) [a]	0.56
$V_{f,tow}$	Tow fiber volume fraction [a]	0.8
n_a	Number of fibers in axial tow (10^3) [b]	24
n_b	Number of fibers in braider tow (10^3) [b]	12
d_a	Diameter of fiber filament in axial tow (μm) [b]	7
d_b	Diameter of fiber filament in the braider tow (μm) [b]	7
L	Length of unit cell (mm) [b]	5.1
θ	Braid angle (degrees)	± 60

[a] Data obtained from Blinzler 2012

[b] Obtained from product data sheets (http://www.toraycfa.com/pdfs/T700SDataSheet.pdf)
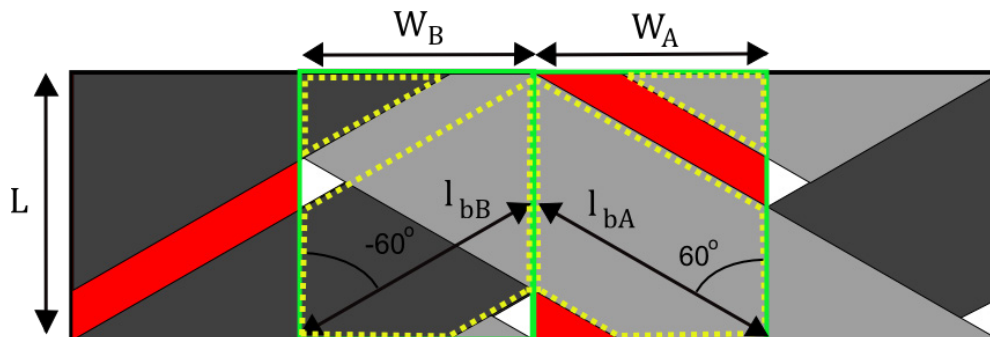

Figure 3.—Two unit cells of the braided composite are shown with the widths of subcells A and B labeled. The green boxes represent the size of a subcell. The dotted yellow boxes represent the amount of a single braider tow contained within each subcell volume (each subcell contains two braider tows), determined by the lengths l_{bB} and l_{bA}. Note: For readability, the dimensions for subcells A are shown in subcell C (above) and it should be noted that both dimensions are identical.
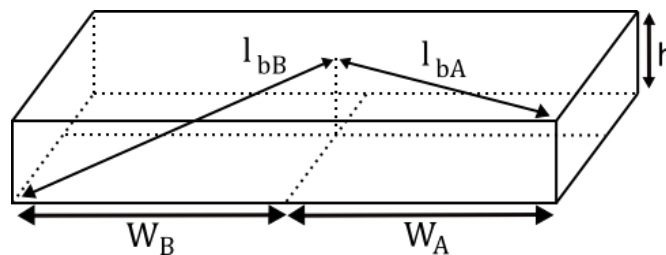

Figure 4.—Schematic of the braider fiber tow lengths approximated by the straight line mode for subcells A and B.

The volume of axial fibers and braider fibers in subcell A are given by,

$$V_{aA}^f = \frac{\pi d_a^2}{4} n_a L \tag{1}$$

$$V_{bA}^f = \frac{\pi d_b^2}{2} n_b l_{bA} = \frac{\pi d_b^2}{2} n_b \left(\frac{W_A}{\sin\theta} \right) \tag{2}$$

The lowercase subscripts *a* or *b* designate axial or braider tow fibers, while the uppercase A or B designate the appropriate subcell. The volume of braider fibers in subcell B is given by,

$$V_{bB}^f = \frac{\pi d_b^2}{2} n_b l_{bB} = \frac{\pi d_b^2}{2} n_b \left[\left(\frac{W_B}{\sin\theta} \right)^2 + h^2 \right]^{0.5} \tag{3}$$

Once the volume of fibers for both the axial and bias directions were known for the respective subcells, the fiber volume fraction and lamina thickness (relative to the total laminate thickness) of the UD plies could be found. First, the volume of the UD ply which represents the axial tow in subcell A, referred to here on as the axial ply, was computed according to

$$V_{aA} = \frac{V_{aA}^f}{V_{f,tow} W_A h L} \tag{4}$$

where V_{aA} is the volume fraction of the UD lamina with respect to the total subcell volume. The equation utilized an assumed fiber tow volume fraction, $V_{f,tow}$, which for the braided T700/PR520 composite was 80 percent (Blinzler 2012). The remainder of subcell A was assumed to represent the braider tow and any pure matrix regions. The UD ply volume fraction for this region was computed by

$$V_{bA} = \frac{1 - V_{aA}}{2} \tag{5}$$

and is hereby referred to as a bias, or braider, ply of subcell A. For any triaxially braided composite, the UD braider plies representing the bias fibers and pure matrix regions in subcells B and D are always evenly partitioned. As mentioned previously, the axial ply was assumed to have a fiber volume fraction equal to that of the fiber tow. The fiber volume fractions of the braider plies, on the other hand, were updated according to

$$V_{f,bl} = \frac{V_{bl}^f}{V_{bl} W_l h L} \quad \text{for } l = A, B \tag{6}$$

where V_{bB} is assumed to be equal to 1. The resulting laminate configurations for subcells A and B are presented in Table 2, where the volume fraction of each ply layer is listed as a percentage of the laminate thickness. As a result of the absorbed matrix model, there are three unique unidirectional plies as indicated by the varying fiber volume fractions listed in Table 2 for the T700/PR520 system.

TABLE 2.—SUBCELL A AND B DISCRETIZATION
FOR THE ABSORBED MATRIX MODEL

Subcell A Lay-up	Angle, °	V_f, %	Thickness, %[a]
Braider ply	−60	73.3	25.5
Axial ply	0	80.0	49
Braider ply	60	73.3	25.5
Subcell B Lay-up	Angle, °	V_f, %	Thickness, %[a]
Braider ply	−60	37.5	25
Braider ply	60	37.5	50
Braider ply	−60	37.5	25

[a] Percent of overall ply thickness

Ply Constitutive Model

The effective unidirectional plies were modeled using the continuum damage mechanics material model MAT 58 within the transient dynamic commercial finite element code LS-DYNA (Hallquist 2006). Based on the Matzenmiller-Lubliner-Taylor theory (Matzenmiller et al. 1995), MAT 58 was selected over other LS-DYNA material models as it allows for nonlinear material response as a function of elastic softening, can be used for the modeling of unidirectional and fabric composites and is available for use in laminated composite shells.

The effective UD plies were assumed to be linear elastic in longitudinal tension and compression, whereas the transverse and shear directions were assumed to be nonlinear. The details for determining the nonlinear behavior will be discussed in the effective UD ply strengths section. As a continuum damage mechanics model, MAT58 employs an exponential damage law to capture the nonlinear response of the composite through elastic softening. The exponential parameters are determined in LS-DYNA based on the user input of failure strength and failure strain and the exponential damage law (Schweizerhoff et al. 1998). The material model specifies the tensile and compressive material strengths and failure strains in the longitudinal (fiber), transverse (matrix) and shear directions, requiring a total of 10 parameters to properly characterize the material response in tension, compression and shear (five stresses and five corresponding strain values).

In MAT58, either a faceted failure surface based on the Hashin failure criterion or a smooth, Tsai-Wu type of failure surface are available. The Hashin criterion was selected to uncouple damage in the transverse and shear directions since the plies do not necessarily represent true lamina and the actual coupling between normal and shear directions is unknown *a-priori*. The next sections discuss the process for determining the initial ply stiffness and appropriate strength properties for the material model.

Effective Unidirectional Ply Stiffness

Since the UD layers and their relative fiber volume fractions are based on the prescribed subcell discretization and not on actual lamina, there are no experimental means by which one can determine their elastic properties. Thus, the mechanical properties of each UD lamina must be computed using a bottom-up micromechanics approach. The microconstituent properties (fiber and matrix) and their relative volume fractions were then utilized to calculate the moduli and Poisson's ratio of the effective UD layers in each of the subcells.

The micromechanics software MAC/GMC 4.0 developed at NASA Glenn Research Center (Bednarcyk and Arnold 2002) based on the Generalized Method of Cells (Aboudi et al. 2012) was used to

compute the effective properties of the UD laminate for this study. Although MAC/GMC was utilized in this work, any appropriate micromechanics software capable of computing effective UD properties would be viable. The bottom-up, micromechanics approach had been proven to be sufficient to characterize the elastic properties of the braided composite (Cater et al 2014, Xiao et al 2011) since the UD discretization of the subcell approach accurately captures the contribution of fibers in the macroscale material coordinate system (particularly for in-plane loading).

The process of determining the UD lamina properties was then repeated depending on the number of unidirectional fiber volume fractions present in the discretization (e.g., in the current braid example there are three unique fiber volume fraction regions as shown in Figure 5). The constituent properties listed in Table 3 along with the fiber volume fractions for the three ply regions were used as input for the MAC/GMC homogenization process. The resulting elastic unidirectional properties for the three different ply regions, identified in Figure 5, are presented in Table 4 for the T700/PR520 system.
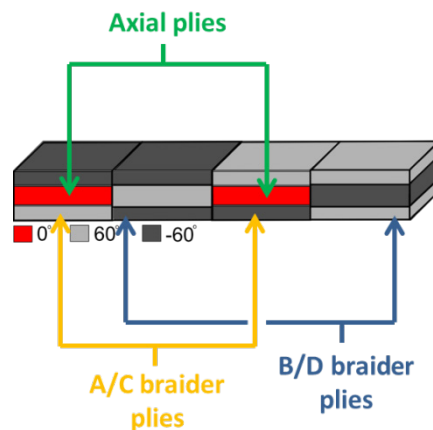

Figure 5.—The absorbed matrix subcell model with the three unique UD ply regions highlighted. The labeled regions (Axial, A/C braider and B/D braider) are UD plies with varying fiber volume fractions.

TABLE 3.—CONSTITUENT MATERIAL PROPERTIES (LITTELL 2008, BLINZLER 2012)

Material	Density, $g\text{-}cm^{-3}$	E_{11}, GPa	E_{22}, GPa	v_{12}	G_{12}, GPa
T700 (Fiber)	1.80	230.0	15.0	0.20	27.00
PR520 (Matrix)	1.25	4.0	4.0	0.38	1.44

TABLE 4.—EFFECTIVE PLY PROPERTIES FOR THE THREE UNIQUE PLY REGIONS (VARYING FIBER VOLUME FRACTION)

Description	UD V_f, %	E_{11}, GPa	E_{22}, GPa	E_{33}, GPa	G_{23}, GPa	G_{13}, GPa	G_{12}, GPa	v_{12}
B-Braider	37.50	88.5	6.22	6.22	2.04	2.86	2.6	0.30
A-Braider	73.30	169.5	9.9	9.9	3.4	8.68	7.0	0.23
A-Axial	80	184.7	10.9	10.9	3.39	10.88	6.0	0.24

Effective Ply Strengths

As a result of the subcell UD discretization, the complex behavior and failure mechanisms of the triaxially braided composite must now be approximated by the response of the UD plies comprising the four subcell regions. A bottom-up approach for computing the UD ply strengths would potentially be inaccurate, since the UD ply mesostructure is a gross approximation of the real tow/matrix regions which would have very different failure mechanisms. The determination of UD ply strengths required a top-down approach where coupon level tests of the braided composite were used to back-out the appropriate ply level strengths of the UD plies in the subcell model. The intent of this top-down approach was to determine the necessary ply strength properties to represent and capture the known mesoscale failure phenomenon observed in braided coupon tests (Kohlman 2012, Littell 2008).

Top-Down Unit-Cell Approach

In order to establish the top-down characterization of UD ply strengths, two key assumptions needed to be addressed.

The first assumption was that experimental strength values (obtained from coupon level tests) are intrinsic material properties unique to the braid architecture and to a specific global loading. By taking macroscopic experimental strengths (i.e., axial tensile strength, axial compressive strength, etc.) as an intrinsic material property, one could now resolve the strength determination problem to a Unit-Cell (UC) problem. The UC for the subcell model consisted of an RUC containing all four subcells, and periodic boundary conditions (PBCs) applied along the boundary to simulate the response of the braided composite. The application of PBCs on the Unit-Cell neglected edge effects associated with finite coupon dimensions, although these effects were present in the actual experiments.

The second assumption was that the main macro- or mesoscopic failure mechanisms observed in the experimental tests could be linked, or approximated to failure of a particular ply. Consequently, the ply strengths could be found by loading the UC to the prescribed macroscopic stress state and determining the level of stress in the "failed" ply. For example, the axial tensile failure of the T700/PR520 braided coupon was dominated by axial tow failure, and the longitudinal strength of the axial plies were calibrated accordingly. Care had to be taken to avoid using experimental coupon tests whose failure was influenced by free edge effects—e.g., transverse, straight-sided tensile tests (Littell 2008) and shear tests (Kohlman 2012) in the triaxial braid—and tests that exhibit multiple, mixed modes of failure.

A schematic of the top-down approach is presented in Figure 6. The proposed workflow assumes that there are no identifiable failures in the experimental test prior to final failure. Material systems and experimental tests which exhibit macroscopic nonlinearity as a function of damage would require additional considerations to the proposed workflow.
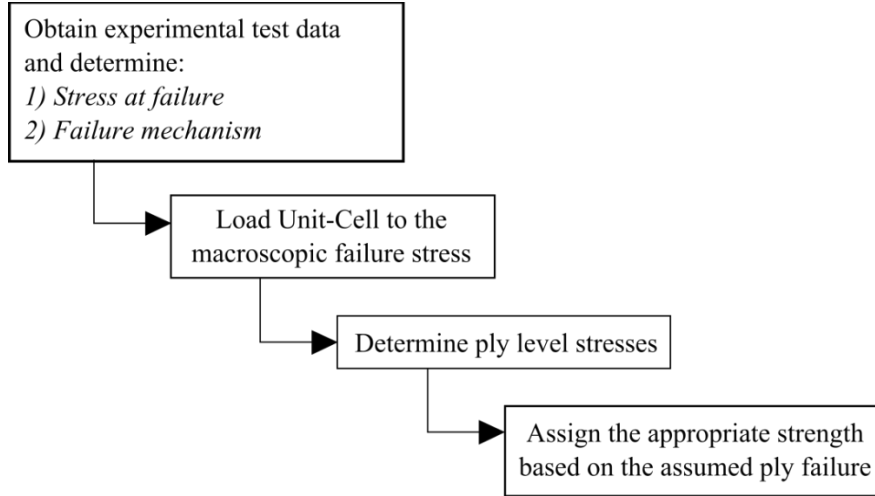
Figure 6.—Workflow of the top-down approach for determining ply level strengths.
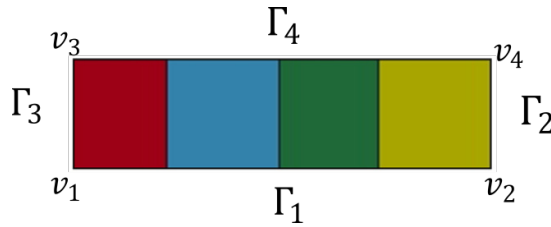

Figure 7.—Unit-Cell (UC) used for the determination
of ply strengths. The vertices and surfaces used
for employing periodic boundary conditions are
identified in the figure.

The UC used for the strength determination process is shown in Figure 7. The application of periodic boundary conditions followed the form presented by van der Sluis et al. (2000) and is represented by Equations (7) below. These nodal constraints were defined in the finite element software through the use of linear constraint equations. The displacements of the vertex nodes are given as v_{xi}, where x specifies the node and $i=1,2,3$ are the displacement degrees of freedom. The only independent vertices are v_2 and v_3. The variable Γ_{xi} corresponds to the displacements along the labeled surface. The first two equations in Equations (7) refer to constraints prescribed between periodic pairs of nodes on opposing surfaces.

$$\Gamma_{2i} - \Gamma_{3i} = v_{2i}, \text{ for } i = x, y, z$$
$$\Gamma_{4i} - \Gamma_{1i} = v_{3i}, \text{ for } i = x, y, z$$
$$v_{4i} = v_{3i} + v_{2i}, \text{ for } i = x, y, z \tag{7}$$
$$v_{1i} = 0, \text{ for } i = x, y, z$$

Based on the coupon level strength results by Kohlman (2012), four experiments were selected to determine the necessary ply strengths in the longitudinal (fiber) direction. These were the axial tensile and compressive tests, notched transverse tensile test, and transverse compressive test. Figure 8 summarizes the identified failure mechanisms in the experimental tests, the prescribed UC loading and the assigned ply failure.
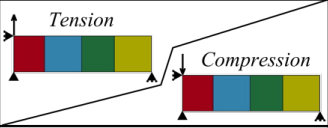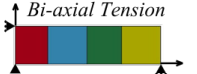
Experimental Test	Failure Mechanism	Unit-Cell Loading	Assigned Ply Failure
Axial Tension (T) and Axial Compression (C)	Axial Tow Failure	*Tension* / *Compression*	Longitudinal Axial Ply Failure (T/C)
Notched Transverse Tension	Braider Tow Failure	*Bi-axial Tension*	Longitudinal Braider Ply Failure (T)
Transverse Compression	Braider Tow Failure	*Compression*	Longitudinal Braider Ply Failure (C)

Figure 8.—Summary of experimental coupon tests used to determine the longitudinal ply strengths.

A limitation of this top-down approach was that failure modes have to be singular and the material response linear-elastic for a given coupon test. Consequently, only coupon tests dominated by longitudinal tow failures could be used to determine ply strengths. The straight sided transverse tensile tests of the braided coupon, for example, could not be utilized; the failure was complex, shear dominated and the coupon response was nonlinear. Two methods were employed to determine the longitudinal ply strength in tension for the braider tows and both are mentioned here in detail.

In the first approach, strength data taken from notched transverse tensile tests (Kohlman 2012) were used to determine longitudinal ply failure of the braider plies in tension as shown in Figure 8. Using high speed imagery, bias tow failures at the gage section of the transverse notched specimen were found to occur during global failure. The notched transverse tensile test, however, created a bi-axial strain state in the braided composite sections, as observed by Kohlman (2012). To utilize the notched transverse tensile data, the reported strains along the gage section of the composite were averaged (in both the loading and perpendicular directions) in order to determine an approximate biaxial tensile load to apply to the unit cell, as shown in the second row of Figure 8.

Due to short comings in the characterization process from the notched transverse tests—presented and discussed later in this paper, a second approach to obtaining the braider ply strengths in the longitudinal direction was developed. In this approach, the bias ply longitudinal failure strains are set equal to the failure strain of the axial plies in the same material direction (1.9 percent). The modulus is then used to compute the appropriate strength. Thus, the bias tow tensile failure strain is assumed identical to the axial tow failure strain. This assumption is supported by the fact that the longitudinal failure of the tows are fiber dominated. It should be noted that the bias UD plies in subcells A and B differed in fiber volume fraction and modulus, thus these strengths were not identical, although the failure strains were set equal.

Bias ply failures for both longitudinal tension and compression were assumed to be independent of their location (e.g., in subcell A or B), therefore the longitudinal bias ply strengths were assigned simultaneously to the braider plies in all subcells. The axial and transverse compressive strengths for the braided composite were obtained from Kohlman (2012) using the standard straight sided coupon tests.

The test matrix in Figure 8 only provided two out of the five required strength data values. Neglected were the transverse tension/compression and shear strengths of the UD plies. These mesoscale failure mechanisms, however, were difficult to observe in the experimental tests (aside from the use of DIC strain data to capture transverse bias tow failure as in Littell (2008)). Additionally, in the standard axial and transverse tension/compression tests of the braided composite, transverse and shear tow failures were not the critical failure mode. Since these subcell ply level strengths could not be determined using the top-down experimental approach, a numerical method was used utilizing micromechanics as discussed in the next section.

Bottom-Up Transverse and Shear Strength

With the aim of initially populating these unknown UD strengths, the following methods/assumptions were utilized to obtain the three remaining strength parameters. First, bottom-up micromechanics was utilized to characterize the nonlinear response of the axial and braider plies in the transverse tensile and shear directions, the two directions dominated by the matrix response. These micromechanics predictions provided the input for the LS-DYNA material model. In these simulations, the fibers were considered linear elastic. For the matrix constitutive response, a nonlinear, strain rate dependent plasticity model which includes the effects of hydrostatic stress was utilized (Goldberg et al. 2003).

First, MAC/GMC was employed using a fiber/matrix representative unit cell to represent the unidirectional effective ply for the three fiber volume fractions determined previously for the braided system (37.5, 73.3 and 80 percent). The MAC/GMC software was used to generate stress-strain curves of the composite ply accounting for the matrix nonlinearity in the transverse and shear directions. The output is shown in Figure 9(a) to (f) for the two loading directions and three fiber volume fractions. Using these stress-strain curves as predicted by the micromechanics, the LS-DYNA MAT 58 strength and strain parameters were determined via curve fitting to the micromechanics predictions.

During the curve-fitting process, the transverse and shear ply directions were both assumed to sustain a constant stress upon reaching a specified strength and strain criterion. The reason for this assumption was the observation from experimental tests that tow splitting/shearing was not a critical failure mode, as the coupon could still carry significant load in the presence of axial and bias tow splits. The addition of a plateau stress in the transverse and shear directions would prohibit significant softening from tow splitting and/or shearing in the simulations. This plateau behavior was prescribed in MAT 58 by specifying a value of 1.0 for the parameters SLIMT2, SLIMC2 and SLIMS, which correspond to the stress limiting value for the transverse tensile, transverse compressive and shear directions, respectively. By comparison, the SLIMT1 and SLIMC1 parameters of the longitudinal directions (tensile and compressive, respectively) were set to 0.01. This relatively small value results in a plateau stress of 1 percent of the specified failure strength, essentially prescribing a brittle failure in the fiber direction.

The appropriate stress and strain values to enter as the transverse strength and corresponding strain for MAT 58 were determined by choosing a point near the plateau of the outputted MAC/GMC curves. An example of this procedure is shown in Figure 9(a), where the dashed lines indicate the value used as the Mat 58 transverse strength and corresponding strain. The plateau stress can be observed in the LS-DYNA results in Figure 9(a), as well as the nonlinear continuum damage mechanics response up to the specified strength.

The failure surfaces in the transverse and shear directions in the current inputs of MAT58 were chosen to be uncoupled by setting the parameter of FC to –1.0. The uncoupled, or faceted failure surfaces allowed for the description of nonlinear shear behavior through the specification of two pairs of stress-strain values, as shown in Figure 10. The material followed the prescribed continuum damage mechanics response up to the specified point TAU1/GAMMA1, after which the material will respond linearly until reaching SC/GMC. With a stress limiting parameter equal to 1.0, the stress will plateau and maintain the limiting stress value of SC. An example of the two points used for specifying the shear response is shown by the dashed lines in Figure 9(b). A comparison of the transverse and shear response of the micromechanics and resulting LS-DYNA MAT 58 material response (determined via one-element verification simulations) for all six cases (two directions and three ply fiber volume fractions) are presented in Figure 9(a) to (f).
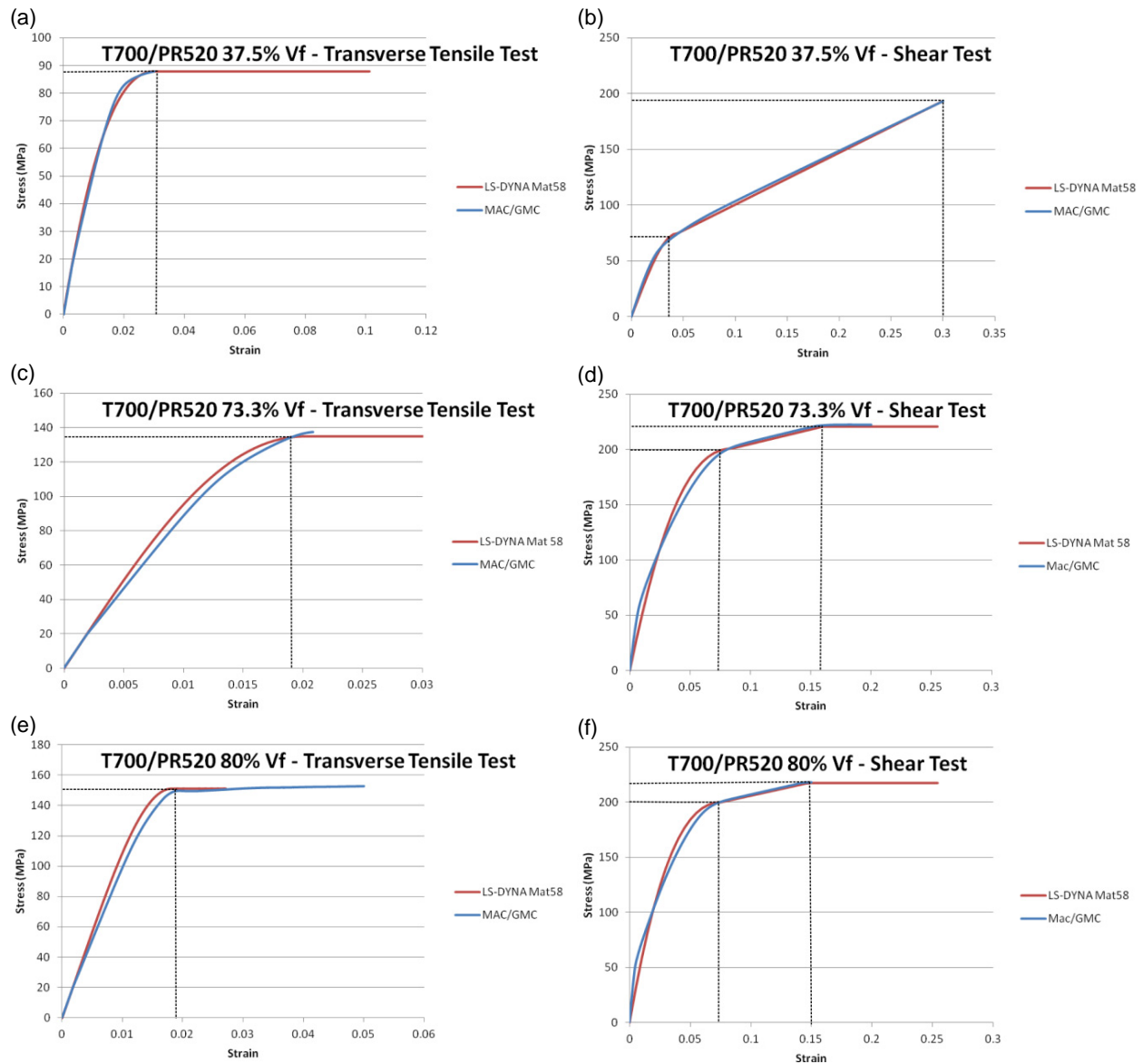
Figure 9.—Comparison of the stress-strain curves output from MAC/GMC and those recreated from one element verification tests in LS-DYNA. Both the transverse and shear stress-strain curves are presented for the three varying unidirectional fiber volume fractions (37.5, 73.3 and 80 percent). The dashed lines indicate the points along the MAC/GMC curves used as input for the LS-DYNA MAT58 material model.

The full set of material strength and corresponding strain values for the T700/PR520 composite are given in Table 5. The MAC/GMC results for the transverse compressive response for all three ply fiber volume fractions did not produce a specific yield point, or nonlinear stress-strain curve to prescribe an appropriate plateau stress, even up to large applied strains of 25 to 30 percent. To overcome this limitation in the prescribed matrix constitutive model, a transverse compressive plateau stress was set equal to the shear strength, and a corresponding strain chosen, based on the transverse ply modulus. This is reflected in Table 5 as the strength values of TC. This assumed compressive strength was assigned to ensure that plies did not hold unrealistically high loads in the transverse compressive directions. It should be noted that this transverse compressive failure of the braider tows was not observed in any of the experiments and may not be a critical parameter.
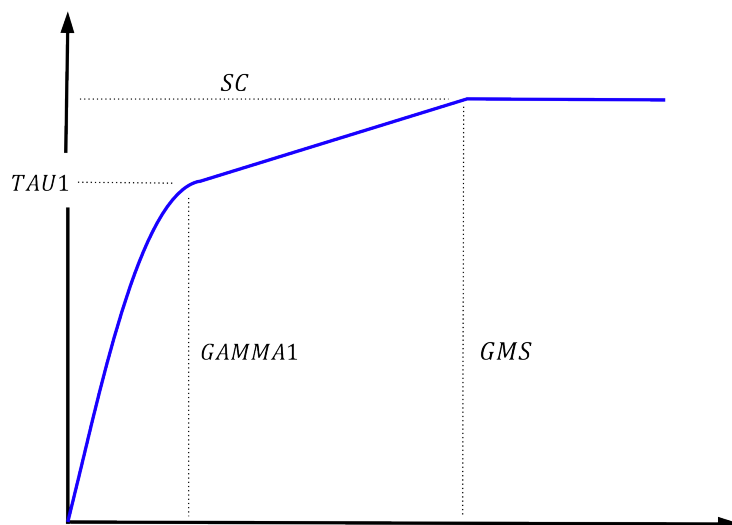
Figure 10.—Shear stress VS strain for Mat 58 when FS=–1.0 (faceted surfaces).

TABLE 5.—UNIDIRECTIONAL PLY PROPERTIES FOR THE T700/PR520 TRIAXIALLY
BRAIDED COMPOSITE IN THE ABSORBED MATRIX MODEL SUBCELL APPROACH

	UD Ply Strength (MPa)						UD Failure Strain		
	LT	LC	TT	TC	SC	TAU1	GAMMA1	ETT2	GMS
Axial Plies	3599	1379	151.0	195.8	195.8	50.0	0.075	0.032	0.1475
A/C Braider Plies	1648	696	135.0	221.0	221.0	201.0	0.084	0.032	0.16
B/D Braider Plies	938	403	87.7	193.4	193.4	75.0	0.045	0.030	0.300

Note: LT = Longitudinal tension, LC = Longitudinal compression, TT = Transverse tension, TC = Transverse compression,
SC = Shear Plateau, TAU1 = First Shear Stress, GAMMA1= First Shear Strain, GMS = Plateau Shear Strain

Summary

This section summarizes the previous discussions for determining the subcell model geometry and material properties. First, the RUC geometry was obtained via microscopy and the necessary ply fiber volume fractions for the subcell discretization are determined using a simple straight line model approach. In the discretization scheme AMM presented here, there were three unique ply fiber volume fractions. Second, the micromechanics code MAC/GMC was utilized to determine the stiffness properties for the different ply fiber volume fractions. In addition, the micromechanics was also used to predict the stress-strain curves in the transverse and shear directions in order to determine the appropriate strength and failure strain parameters for LS-DYNA's MAT 58 material model. Lastly, a top-down approach with a periodic unit cell method was used to take experimental strength and failure strain data in the longitudinal and transverse braided coupon directions and determine the subcell, ply level longitudinal strengths.

Experimental Setup

Off-axis tension testing on composite specimens was conducted at the NASA Glenn Research Center in Cleveland, Ohio. The purpose of the testing was to provide additional material characterization of the braided composite as well as validation test cases for the subcell modeling approach. Testing was completed with off-axis orientations of 0°, 30°, 45°, 60°, and 90°. The 0° and 90° represent the standard

axial and transverse coupon tests used to characterize orthotropic materials. The 30° and 60° directions were chosen, as they are aligned perpendicular and parallel, respectively, to the bias fiber tows. The 45° test, similar to the 90°, is not aligned with a fiber tow. The results presented here are for the T700/PR520 composite system.

Mechanical Testing

The mechanical testing was conducted on an MTS servo-hydraulic axial torsion test frame with axial full-scale capabilities of 220 kN. The specimens were gripped in MTS 647 wedge-style grips with Surfalloy coating. Mechanical stops were located on the grip wedges to ensure proper and consistent specimen alignment throughout the testing. For all testing, two inches of the specimens at the top and bottom were gripped with maximum machine grip pressure. Maximum grip pressure was used to prevent specimen slip in the grips during testing. No tabs or abrasive paper were used on the specimen grip areas during testing. All testing was completed at a crosshead displacement rate of 0.021 mm/s. A typical test specimen gripped in the test frame is shown in Figure 11.

Digital Image Correlation

Subsets of the test specimens were monitored with digital image correlation (DIC) using GOM's ARAMIS system. DIC is a noncontact method for the evaluation of full-field 2D and 3D surface strains. For DIC measurement, a random, high contrast speckle paint pattern is applied to the surface of the specimens. In this work, a standard spray paint was used. The speckle pattern deforms with the specimen. Through the analysis of successive images, the DIC software can generate the local displacement distribution of the viewing field and compute strain components.

The coupon axial strain value was determined using a 25.4 mm "virtual" axial strain gage provided within the ARAMIS software. This axial gage was centered on the specimen and was used to compute the elastic modulus and construct the stress-strain curves of the specimens. At least three specimens were tested; however, not all were analyzed using the full field data. A representative image of the test setup for the digital image correlation is shown in Figure 12.

Besides as a strain measurement technique, the DIC measurements also provided information on the identification of damage initiation and evolution to failure through the use of the full field strain data. This data provided understanding of the progressive failure patterns and regions of localized strains.

Figure 13 presents the representative full-field surface strain images for a 60° off-axis specimen under tension. The axial strain and transverse strain are pictured, where the axial direction is aligned with the global loading direction.

Experimental Results

The experimental results are organized to compare and contrast all five experimental coupon directions. First, the reported moduli and strength values are discussed to understand the trends in the macroscopic data such as the modulus and ultimate strength of the coupon based on loading orientation. Second, a study of the local failure morphologies for each material direction is presented to compare the cause of catastrophic failure in each test. Last, the full field strain data from the digital image correlation are presented in order to identify regions of localized cracking and damage, which may explain the variation of failure modes and the observed trends in measured strength with coupon orientation.

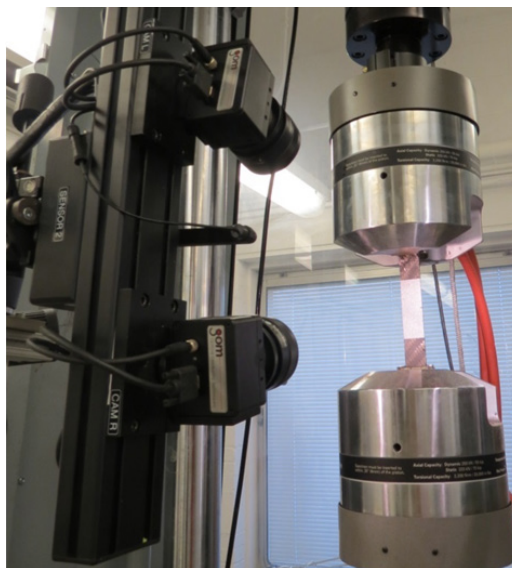Figure 11.—Typical specimen gripped in test frame.

Figure 12.—Photogrammetry cameras setup to view typical off-axis tension test.
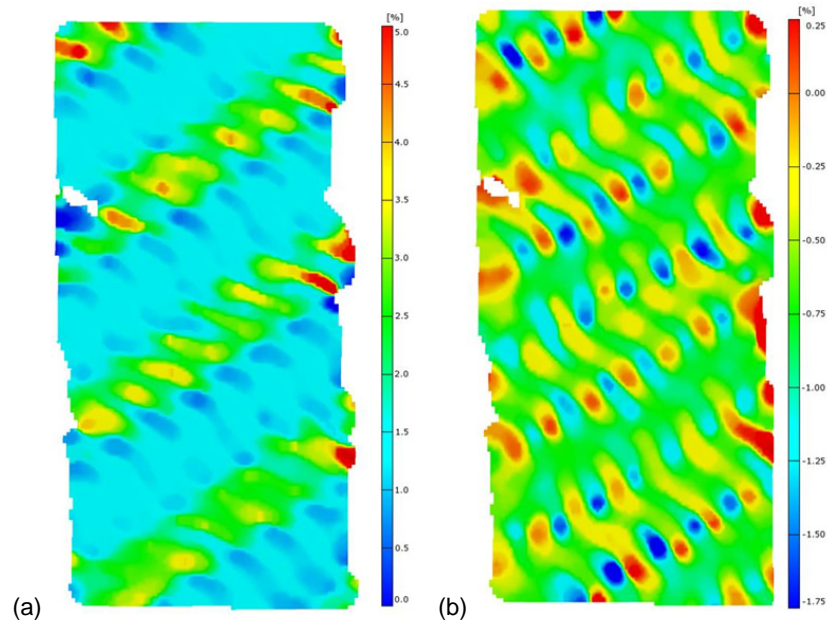
Figure 13.—(a) Axial strain for 60° off-axis specimen and (b) transverse surface strain for 60° off-axis specimen under tension.

Coupon Moduli and Strengths

The measured moduli for the various off axis coupons are provided in Figure 14. As expected, both the 0° and 60° coupons exhibited the highest stiffness, since both coupons have tow continuity between the mechanical grips. The remaining coupons, which do not have tow continuity, had similar moduli values with respect to each other. Aside from the 13 percent variation between the highest and lowest moduli values, the material remained relatively quasi-isotropic in plane as expected due to the 0°/±60° braiding pattern. The stress-strain response of the 0° and 60° coupons were linear elastic until failure. The remaining three off-axis coupons, conversely, exhibited nonlinearity prior to failure. The stress-strain curves for each test angle are shown in Figure 15.

The strengths, on the other hand, differed significantly across the off-axis angles as shown in Figure 15. The strength data is summarized Figure 16. The 0° coupon had the highest reported strength at 984 MPa. The 60° coupon exhibited a 12 percent reduction. The 45° and 90° coupon had strength values merely a half of the axial strength of the braided coupon at 557 and 560 MPa, respectively. The 30° coupon was the worst performing in terms of ultimate strength, with a value of 488 MPa. The scatter in the measured strength values can be attributed to the variation of failure modes associated with each orientation. In addition, the low strength values of the 30°, 45° and 90° coupons were accompanied with nonlinear stress-strain behavior as seen in Figure 15. The failure morphology and failure mode for each test is described in the next section.
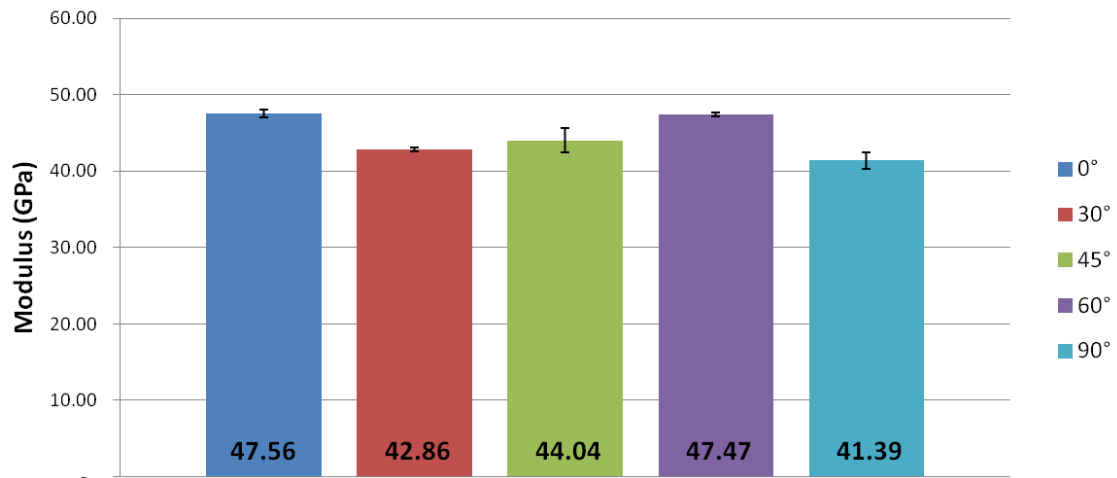
T700/PR520 Off-Axis Modulus

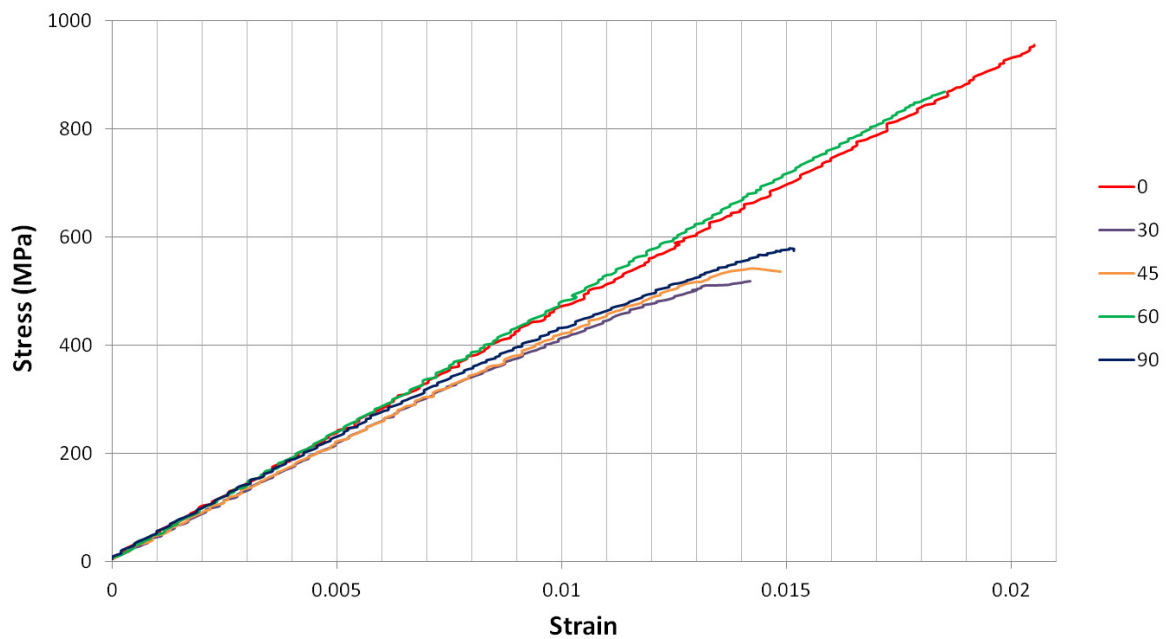Figure 14.—Measured elastic moduli from the off-axis coupon tests.

Figure 15.—Stress-strain curves for the off axis tensile coupon tests. Note: Only one experimental stress-strain curve is displayed for each angle.
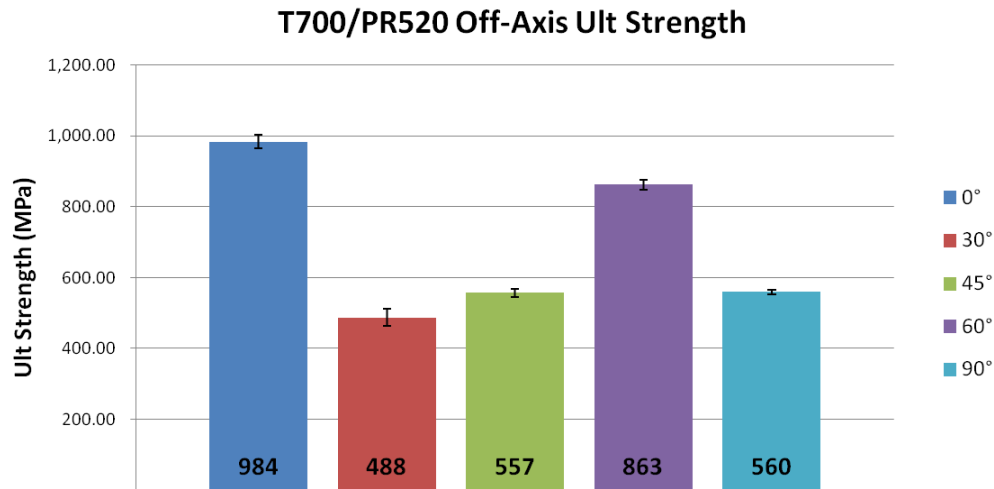
T700/PR520 Off-Axis Ult Strength

Figure 16.—Measured strength values from the off-axis coupon tests.

Failure Morphology

Coupons of the braided composite tested at different on- or off-axis orientations exhibit distinctively different failure morphologies. The reason for the analysis of the failure morphology was to understand the cause of the significant variation in mechanical properties measured in these specimens. The failure morphologies of the tested coupons are summarized in Figure 17.

The 0° and 60° coupons, which exhibited the highest strengths, had the most catastrophic failure and exhibited a minimal residual stiffness/strength after reaching the peak load. Furthermore, the 0° and 60° coupons often had additional compressive failures observed near the grips, which may be a result of the rebounding, post-failure stress wave from the coupon gage section. In both cases, the final failure mechanism was identified as tensile failure of the tow lying parallel to the loading direction. In the 0° coupon, this was the axial tow, whereas for the 60° coupon it was the corresponding bias tow. The failure path in the 0° coupon was transverse to the loading direction, perpendicular to the axial tows as shown in Figure 17(a). The red dashed line in the figure represents the failure path. The 60° coupon failed in a path preferential along the axial tows (at a 60° angle), as shown in Figure 17(d).

The 30° coupon was unique such that it exhibited the highest post-failure residual stiffness (qualitatively) as compared to other coupons. As seen in Figure 17(b), the only observed tow failure was of the bias tows lying perpendicular to the loading direction. The fractured surface is rather clean, as indicated by the arrow in the enlarged insert. On the other hand, the tows that did not fracture underwent shifting and pull-out, as seen in the axial tows and other bias tows. The failed, perpendicular bias tows were under compression due to the overall Poisson contraction of the coupon with the macroscopic loading. The clean fracture surface (unlike the frayed fiber tow ends in the tensile failures) is also indicative of compressive failure of these bias tows. The path of bias tow compressive failures were aligned with the axial tow, as seen by the dashed line in Figure 17(b), at the point of undulation for the failed bias tow.

Unlike the previous three test cases, the 45° coupon did not exhibit a failure clearly associated with the tensile or compressive failure of a specific tow direction. In Figure 17(c), the bias tows near the failed gage section show diffuse splitting and pull-out from the edges of the coupon and several axial tow segments (hidden by the braider tows) had clearly fractured. Since these axial tows oriented 45° degree to the tensile direction, it is hypothesized that the failure of the axial tow is associated with a shear dominated, or a combined failure in conjunction with bias tow failures initiated from the free edge. Unlike the other cases, a definite failure path could not be determined for the 45° coupons.
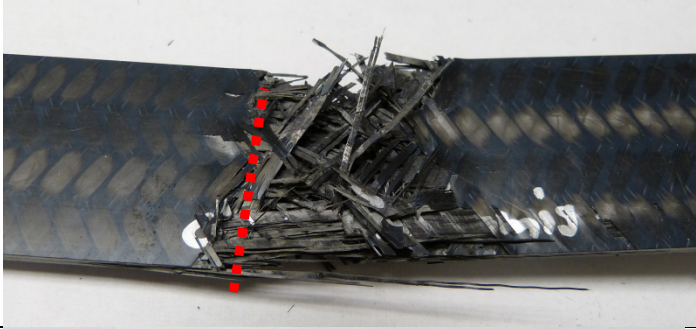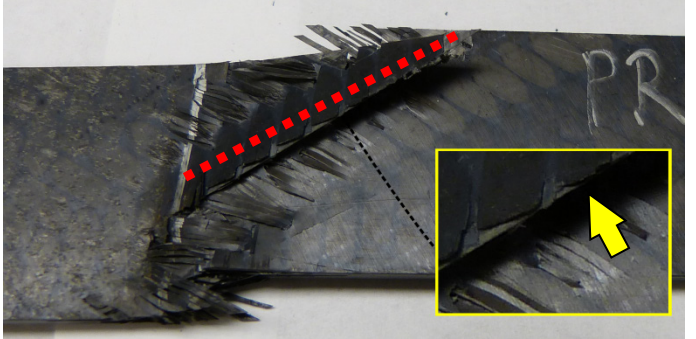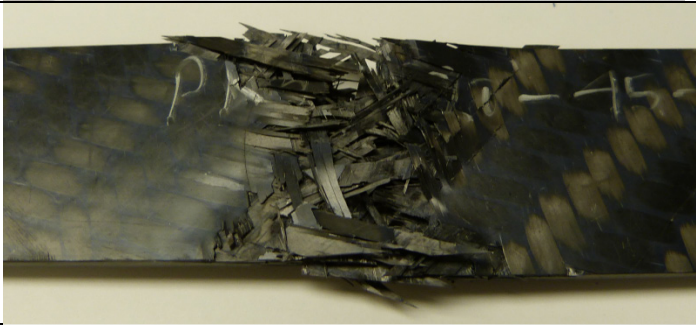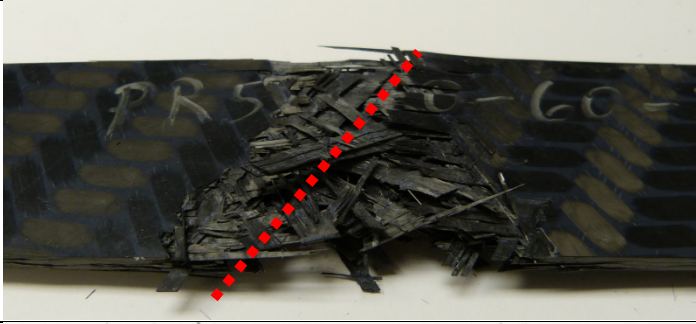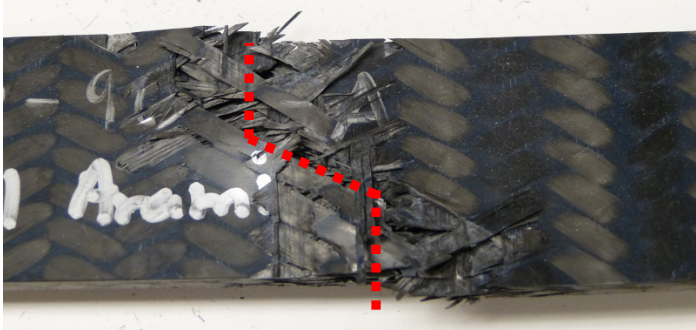
(a) 0° Tensile Test **Failure Notes**: Longitudinal failure of the axial tows. Catastrophic failure with minimal remaining coupon strength. Failure path looks to be concentrated perpendicular to the loading and axial direction.	
(b) 30° Tensile Test **Failure Notes**: Compressive failure of the bias tows lying perpendicular to the applied loading. The failure path of the compressive bias tow failures are along the axial tows and at the point of undulation. The other bias and axial tows remain continuous.	
(c) 45° Tensile Test **Failure Notes**: No obvious failure of a specific axial or braider tow. Failure pattern is similar to that of the 90° coupon in that edge damage and shearing look to be a present phenomenon. Shear failure of the axial tow fibers were observed.	
(d) 60° Tensile Test **Failure Notes**: Catastrophic failure due to longitudinal failure of the bias tows parallel to the applied loading. The main failure path tends to lie along the axial tow path.	
(e) 90° Tensile **Failure Notes**: Highly edge initiated shear failure. Damage occurs and initially propagates along the axial tow path, perpendicular to the loading direction, but in nearly all specimens jumps to an adjacent axial tow path due to the local shearing of the axial fibers.	

Figure 17.—Images of the failed braided coupons along with general notes on failure mechanism.

The 90° coupon displayed failure morphologies consistent with those described in Kohlman (2012). The damage was initiated at the free edge, which caused a shear failure. The damage initially was along the axial tow path; however, it jumped to an adjacent axial tow path. An image of the failure is presented in Figure 17(e). This phenomenon is likely due to the occurrence of initial cracking at two different locations on the opposing free edges, documented by Kohlman as edge-initiated damage. The two regions met through the shear failure of an axial tow and led to the final failure, as shown by the dashed red-line in Figure 17(e).

Digital Image Correlation Results

In this section, the full field strain data from DIC are presented. Two sets of strains: the axial strain and transverse strain which are oriented parallel and perpendicular to the load, respectively, are shown. The axial and transverse strains are also labeled as Epsilon X and Epsilon Y, respectively, in the DIC plots. The images presented are the last frame available prior to specimen failure. The purpose of this investigation was to understand the influence of damage localization or edge effects prior to final failure.

Figure 18(a) and (b) shows the axial and transverse strains for the 0° coupon. The concentrated regions of 2.25 to 2.75 percent strain shown in Figure 18(a) coincide with the location of bias tows at the surface of the specimen. The high axial strains are indicative of bias tow splitting, or microcracking of the matrix within the fiber tow. These cracks can also be observed visually in the post-mortem specimens. These cracks were observed previously in the experimental work of Littell (2008). In both Figure 18(a) and (b), there are no distinct high-strain regions near the edge of the coupon which would indicate any edge initiated damage.

The 60° coupon, whose DIC results are shown in Figure 19(a) and (b), also show signs of bias tow splitting. This can be seen from the high axial strains in Figure 19(a) which coincides with the location of surface bias tows. In the 60° coupon, the splitting appears less diffuse as it does in the 0° coupon, affecting only the bias tows not aligned with the loading direction. While there may be axial tow splitting as well, this damage mode is not visible from visual inspections or the DIC strain data. Although some of the transverse strains shown in Figure 19(b) are concentrated at the edge, further observations show they are likely caused by localized cracking of bias tows at the free edge. This edge damage, however, does not play a role in the main tensile failure of the bias tows aligned with the loading direction.

The DIC results for the 30° coupon are shown in Figure 20(a) and (b). High strain regions localized near the edge of the coupon in the DIC images can be seen in the axial strain, shown in Figure 20(a), and the transverse strain in Figure 20(b). Cracks were observed in the bias tow located above the axial tow and may be the source of the localized strain at the edges. Preferential cracking is seen along the axial tow direction in both cases, and the alignment of these high strain regions in Figure 20(a) coincide with the failure path observed in the coupon. It is not clear whether the observed edge cracking in the transverse bias tows was an initiator of premature failure. The DIC results prior to final failure do suggest, however, that the bias tow compressive failures were initiated at the edge.

The DIC results are presented for the 45° coupon in Figure 21(a) and (b). Similar to the 30° coupon, highly localized axial strains near the free edges of the coupon indicate edge initiated damage. Bias tow splitting, caused by local matrix cracking within the tow, can be observed in Figure 21(a) as the 2.1 percent strain bands oriented nearly transverse to the loading direction. This cracking can be observed visually as well on the top and bottom surfaces of the coupon. The failure morphology of the 45° coupon discussed previously indicates a possible edge shearing damage similar to that observed in the 90° tests. The localization of strain at the edges observed in the DIC plots supports that suggestion.

(a)

Axial Direction

Transverse Direction

Load Direction

2.750e+00
2.550e+00
2.350e+00
2.150e+00
1.950e+00
1.750e+00
1.550e+00
1.350e+00
1.150e+00
9.500e-01
7.500e-01

(b)

Axial Direction

Transverse Direction

Load Direction

0.000e+00
-1.250e-01
-2.500e-01
-3.750e-01
-5.000e-01
-6.250e-01
-7.500e-01
-8.750e-01
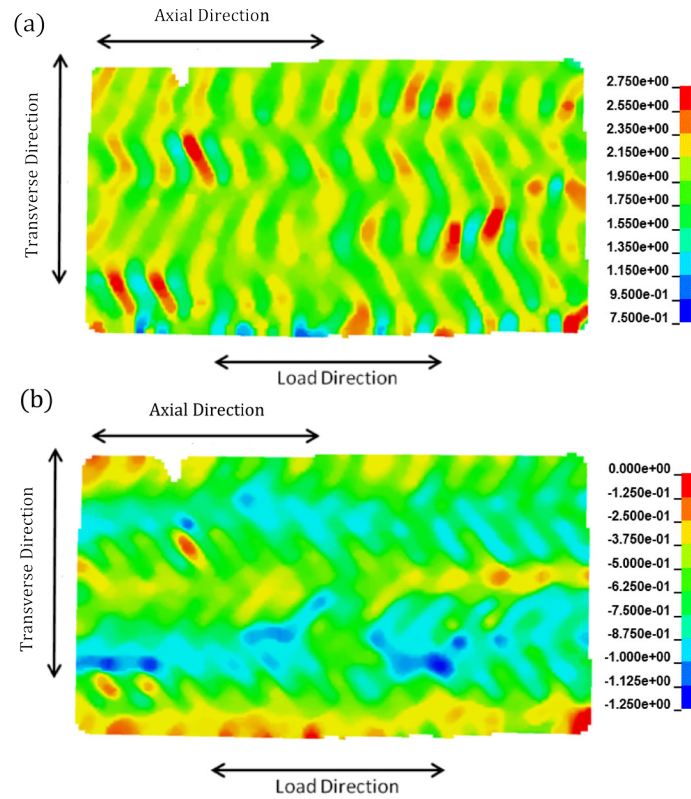-1.000e+00
-1.125e+00
-1.250e+00

Figure 18.—DIC Images of (a) axial strain (parallel to the labeled loading direction) and (b) transverse strain (perpendicular to the labeled loading direction) for the 0° coupon under tension prior to final failure.

(a)

Axial Direction

Transverse Direction

Load Direction

%
3.250e+00
2.950e+00
2.650e+00
2.350e+00
2.050e+00
1.750e+00
1.450e+00
1.150e+00
8.500e-01
5.500e-01
2.500e-01

(b)

Axial Direction

Transverse Direction

%
-1.388e-16
-1.000e-01
-2.000e-01
-3.000e-01
-4.000e-01
-5.000e-01
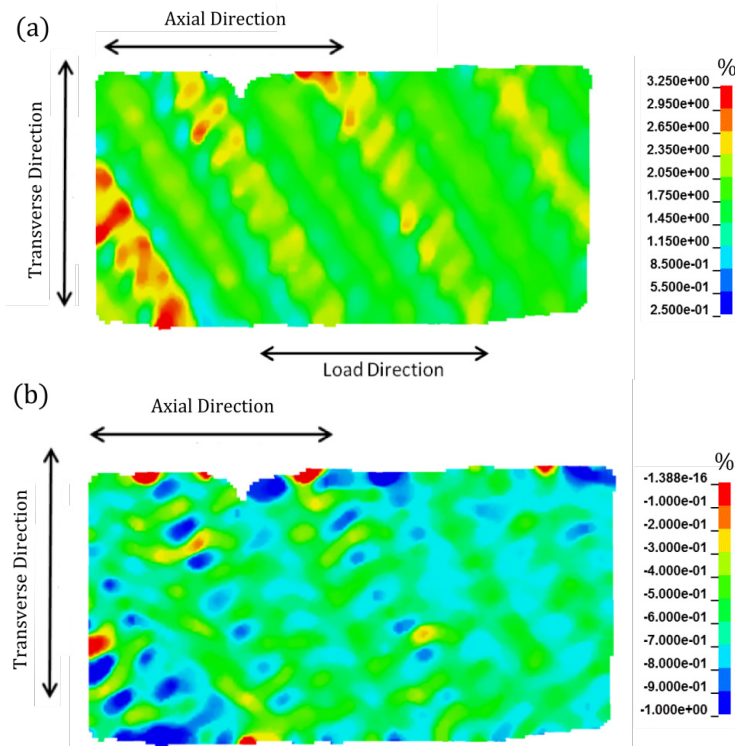-6.000e-01
-7.000e-01
-8.000e-01
-9.000e-01
-1.000e+00

Figure 19.—DIC Images of the axial strain (a) and transverse strain (b) for the 60° coupon under tension prior to final failure.
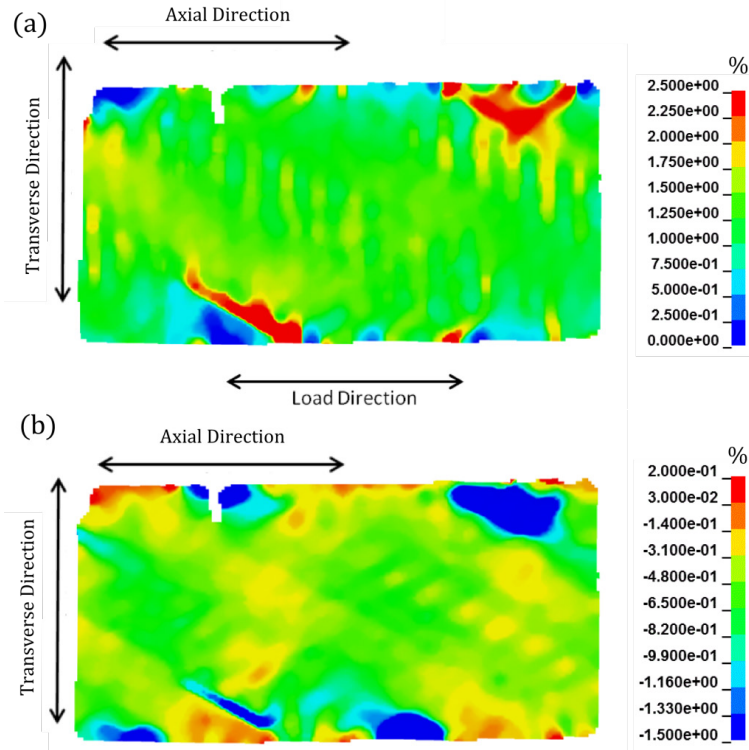
Figure 20.—DIC Images of axial strain (a) and transverse strain (b) for the 30° coupon under tension prior to final failure.
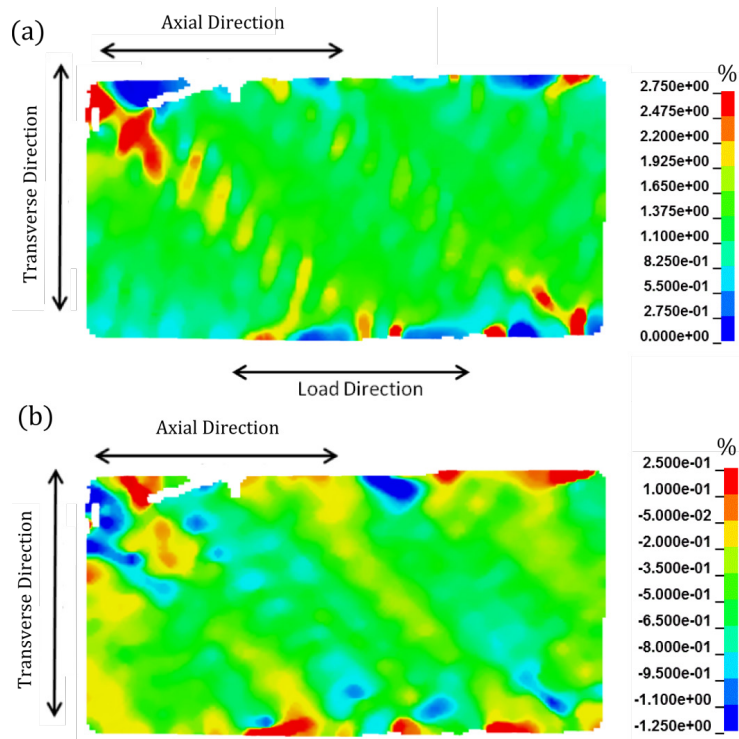

Figure 21.—DIC Images of axial strain (a) and transverse strain (b) for the 45° coupon.

(a)

Axial Direction

Transverse Direction

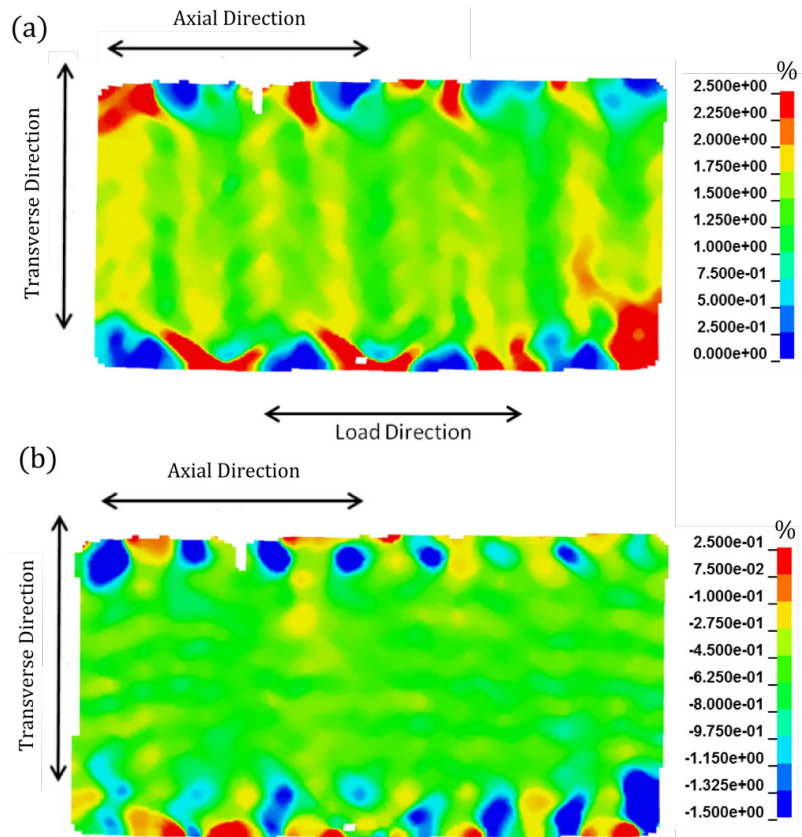Load Direction

(b)

Axial Direction

Transverse Direction

Figure 22.—DIC Images of the axial strain (a) and transverse strain (b) for
the 90° coupon under tension prior to final failure.

Figure 22(a) and (b) present the axial and transverse strain contours for the 90° coupon. The 90°
coupon exhibits high strain localization at the free edge which is more diffuse and widespread than in the
other off-angle directions, occurring periodically over the observed length. Previous experimental work
(Kohlman 2012) noted that the damage of the coupon initiated at the edges in locations similar to those
showing the highest axial strain. The current DIC results indicate that the highest strain regions are at the
intersection of bias tows (between the axial tows).

Finite Element Model

In the discussion to follow in the remainder of this report, only the 0°, 30°, 60° and 90° coupons are
discussed. The 45° coupon will be used for final validation of the subcell modeling approach and will not
be utilized during this initial verification phase, where it is anticipated that model parameters will be
modified/changed to match the physical response of the braided composite. The results of simulations of
the 45° coupon will be presented in another report focused on the validation of the subcell approach.

The finite element mesh follows the subcell modeling approach, whereby each individual subcell is
assigned to a unique composite shell element which contains the appropriate UD stacking and
orientations. In LS-DYNA, this is accomplished through the use of the *Section_Shell keyword to specify
the number of layers and orientations, and the *Integration_Shell keyword to specify the material and
thickness of each integration point, which in the subcell modeling approach is tied to a given UD layer.
Belytskcho-Tsay conventional shell elements were used. The FE mesh is shown in Figure 23, where the

0° and 90° meshes are similar to previous subcell works (Goldberg et al. 2010). For the 30° and 60° coupons, the subcell mesh is skewed, as shown in Figure 23, to accomplish the following goals:

1. Preserve quadrilateral elements along the free-edge boundaries of the coupons
2. Preserve the orientation of the axial tows which are dictated by the red and green element paths shown in the FE mesh

Since free-edge failure was a common, observable phenomenon in the 45° and 90° coupons, measures were taken to ensure that stress-strain calculations at the free-edges would not be distorted by triangular or poorly formed elements. For 30° and 60° coupons, triangular and poorly formed elements do exist at the grip boundaries (not shown). Failure in these regions would invalidate simulation results. Consequently, artificially high strength values are imposed on all elements which are triangular at the gripped boundary or are poorly conditioned. As a result, these regions would behave orthotropic elastic through the entirety of the simulation and force failure to occur away from the gripped boundary. This meshing approach at the gripped boundaries does not conflict with experimental results, since the 30° and 60° coupons failed predominantly at the gage section of the coupon.

The second assumption was made in order to preserve the orientation of the subcell modeling approach, which was preferentially aligned with the axial tow direction. To account for the skewed nature of the subcells, the subcell area was preserved to ensure that the characteristic length associated with the subcells would be consistent across all of the simulations (0° through 90°), thereby eliminating any influence of element size when comparing the simulation results. In general practice, this method of skewing the subcell orientation need only be performed when it is necessary to create a "clean" boundary which does not lie parallel or perpendicular to the axial tow path.
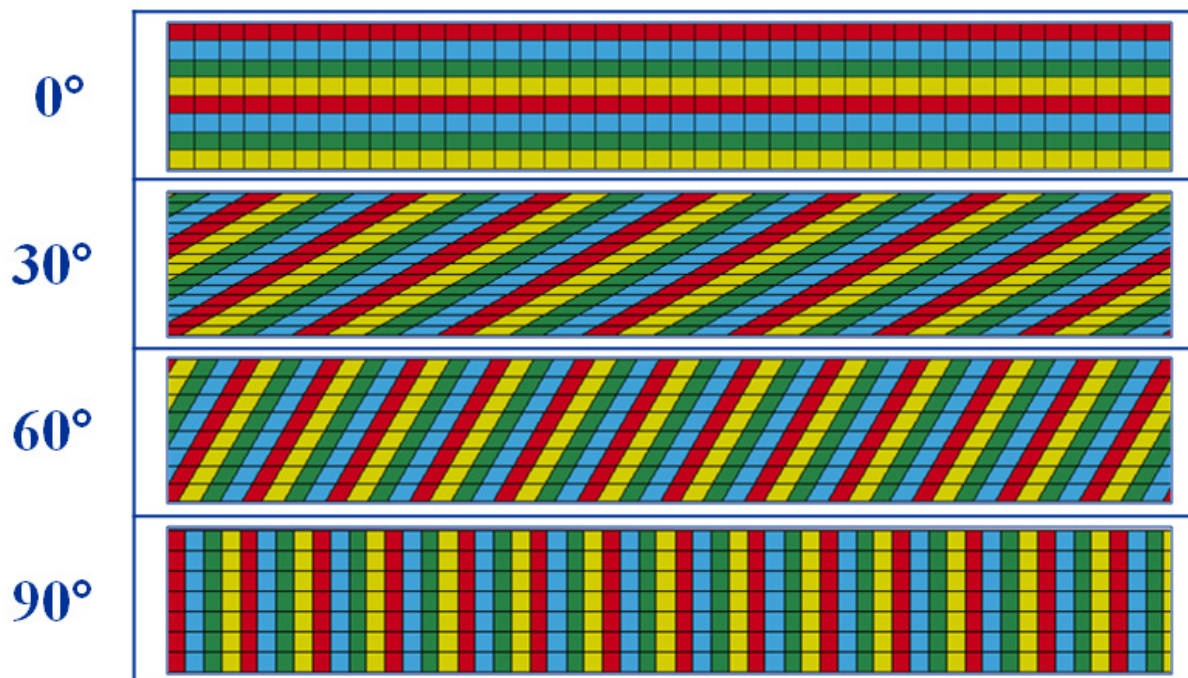

Figure 23.—FE mesh of the various off-axis coupons simulated in LS-DYNA. The color coding represents the unique subcell regions (A=Red, B=Blue, C=Green, D=Yellow).

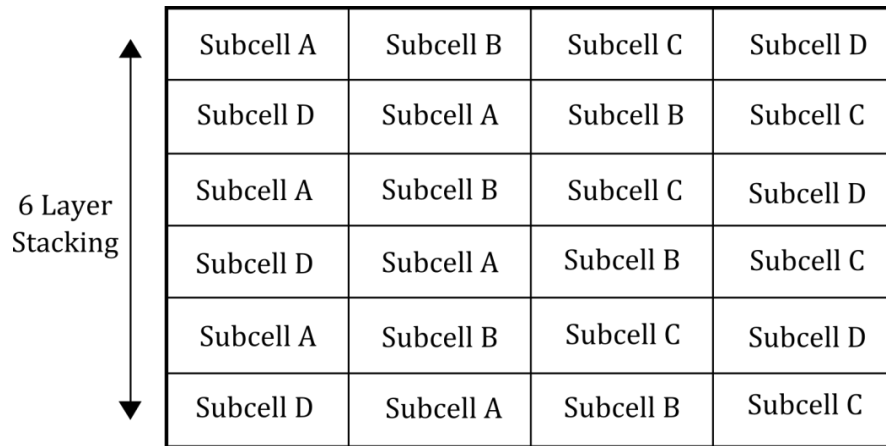| Subcell A | Subcell B | Subcell C | Subcell D |
Subcell D	Subcell A	Subcell B	Subcell C
Subcell A	Subcell B	Subcell C	Subcell D
Subcell D	Subcell A	Subcell B	Subcell C
Subcell A	Subcell B	Subcell C	Subcell D
Subcell D	Subcell A	Subcell B	Subcell C

6 Layer Stacking

Figure 24.—Schematic of the through-thickness ideally shifted coupon stacking.
Each row represents a braid layer. The ideally shifted stacking configuration
features shifting of the axial subcells (A and C) through the thickness.

Previous works (Cater et al. 2014) found that using a single shell element to represent a multi-layer braided coupon did not accurately predict the transverse (90°) modulus of the coupon nor capture the effects of the locally unsymmetric areas. Thus, the six layers of the braided composite were modeled by individual shell layers in this current work. Two different stacking orientations were investigated (perfectly stacked and ideally shifted) as was done in previous subcell studies (Cater et al. 2014). The first configuration assumed that axial tows were aligned perfectly through the thickness, whereas the shifted model assumed that an every-other nesting was occurring between the axial tows. A schematic of the ideally shifted model is shown in Figure 24, showing the alternating subcells through the thickness of the coupon. It was found formerly that the two stacking configurations affected the predicted transverse modulus slightly; however, there were no obvious results to conclude preferring one stacking arrangement over the other.

In addition to the nesting configuration, the appropriate contact definition between the various plies was investigated. In previous works, a tiebreak contact was employed between shell layers. Nodal constraints would be applied with respect to the translational degrees of freedom only, but would allow for the failure/separation of the nodal constraints upon reaching a failure criterion. This contact definition is hereby referred to as "tiebreak". The second formulation was a shell-edge to surface constraint which can be applied between node sets along a shell edge and a surface segment. This constraint ties the rotational degrees of freedom and translational degrees of freedom between the shell element nodes and the displacements and curvatures of the respective surface. When applied between the conventional shell layers along with an option to consider distance offsets, it constrains both the rotational and translational degrees of freedom of the two layers. This second contact definition, however, does not allow for failure or separation between layers, and is hereon referred to as the beam offset contact type.

The two contact types will be investigated, along with the two stacking configurations, to understand the influence of each on the coupon behavior and determine the appropriate considerations to take for future impact analysis. No failure is prescribed in the tiebreak contact. The material and model parameters for the T700/PR520 composite are taken as presented from the previous sections on Subcell Modeling.
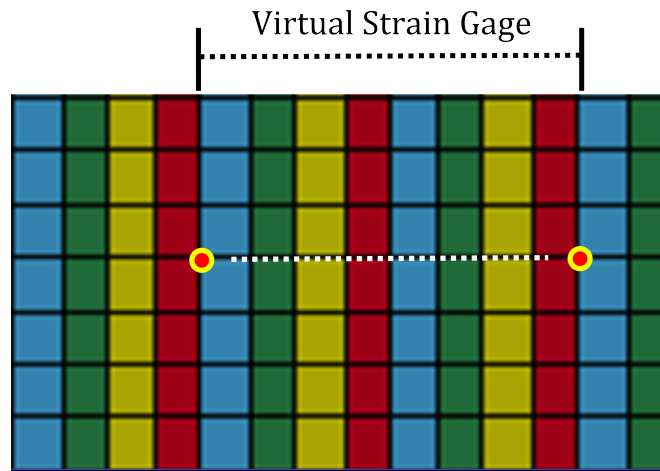
Virtual Strain Gage

Figure 25.—FE mesh of the 90° coupon showing the positioning
of the virtual strain gage (note: only a portion of the FE mesh
is shown, and loading is applied in the horizontal direction).

Simulation Results and Discussions

The results from the numerical FE model are presented in this section. All strain results were obtained from the LS-DYNA simulations via the use of a virtual strain gage, shown in Figure 25. The virtual strain gage was based on the nodal displacements of two nodes located at the mid-section of the coupon. The distance between the two nodes were two unit cells in length (approximately 35.6 cm). The stresses were determined via reactionary forces at the applied boundary condition (in the load direction).

Shell Contact and Subcell Stacking Configuration Study

The first set of numerical simulations consisted of both the two contact definitions between the individual shell layers and the two stacking configurations discussed in the previous section. The results from the 0°, 30°, 60° and 90° coupons are discussed in what follows; however, for brevity not all stress-strain curves are shown. These first set of tests were used to determine the best contact and stacking configuration to use in future studies. As such, these first set of results discussions will cover the comparison between stress-strain curves of the FE simulations and experimental results. In a later discussion, the comparison between experimental and numerical failure mode predictions on the final coupon configurations will be presented. In addition, this first investigation utilizes only the bias ply longitudinal strengths determined from the top down unit-cell approach discussed in previous sections.

The predicted strength of the axial (0°) coupons were found to be sensitive to the stacking configuration, with estimations of 892 MPa and 904 MPa for the ideally shifted and perfectly stacked configurations with tiebreak contact, respectively. These values are both slightly lower than the experimentally reported value of 984 MPa. Both the experimental and numerical stress-strain curves were linear elastic until failure, with the simulations showing some nonlinearity immediately before failure. This nonlinearity, however, was simply a function of the exponential form of damage evolution in the continuum damage mechanics model (MAT 58 in LS-DYNA). The results for the 0° coupon also showed minimal sensitivity with respect to the contact definitions. The tiebreak and beam offset coupons displayed minute differences in moduli and strength for the same stacking configuration.
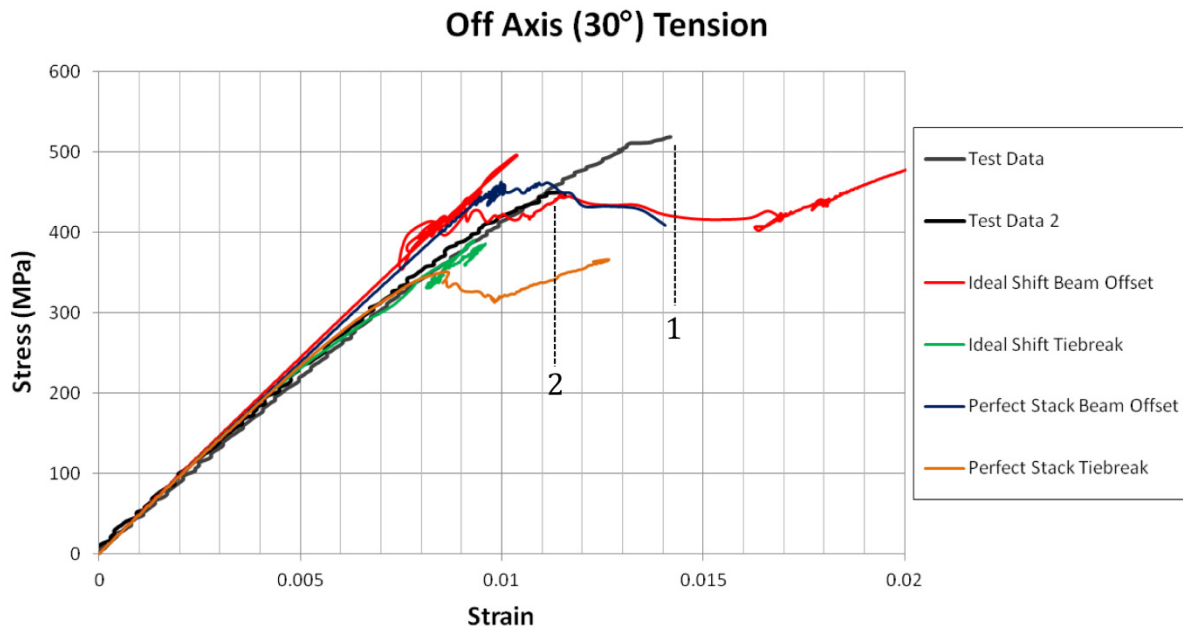
Off Axis (30°) Tension

Figure 26.—Stress-strain curves for the 30° coupon test for both contact types and stacking configurations. The experimental data is shown in gray and black and numbered in the figure. The colored lines represent the four simulation coupons with varying stacking or contact type as indicated in the figure legend.

The results from the 30° coupon are shown in Figure 26 for all four coupon types alongside the experimental data. The estimated strength of the coupon was found to be insensitive to the stacking configuration as shown below. For example, both the ideally shifted and perfect stack coupons with the beam offset contact definitions exhibited similar ultimate strengths and ductile post-peak responses. The choice of contact type, however, affected the coupon response and ultimate strength. The predicted strength of the 30° coupon with the beam offset contact (488 MPa) compared well with the test data (518 and 455 MPa). The coupon with beam offset contact was linear to the predicted strength. The tiebreak coupons, on the other hand, exhibited a nonlinearity in the stress-strain response seen in the experimental tests. The tiebreak contact, however, caused premature failure well below the experimental values. The perfect stack tiebreak coupon, for example, predicted a strength value 20 percent lower than the lowest experimental strength.

The 60° coupon tests were found to be sensitive to both the contact definition and stacking configuration. All simulation results, however, were found to under-predict the experimental strengths by nearly 50 percent in all four test cases. Due to this large discrepancy, the simulation results are not valuable in producing meaningful conclusions on proper contact definition or stacking configuration and are excluded here. In addition, the large under-prediction highlights a deficiency in the initial method used to determine the tensile strength of the bias plies. In the section to follow, the results for the 60° coupon will be presented using the second method to obtain a bias tow longitudinal strength and will be compared to the initial top down unit-cell approach.

The stress-strain curves from the transverse, or 90°, coupon simulations are shown in Figure 27, along with the experimental test data. Similar to the 30° coupon, the resulting predictions were found to be sensitive to the type of contact defined between the layers. The tiebreak coupons exhibited earlier softening in the material response, due to the yielding (in the transverse and shear directions) in some localized regions in the subcells. They also displayed lower estimated strengths than their beam offset coupon counterparts. The transverse coupon results also present a strong difference in coupon response
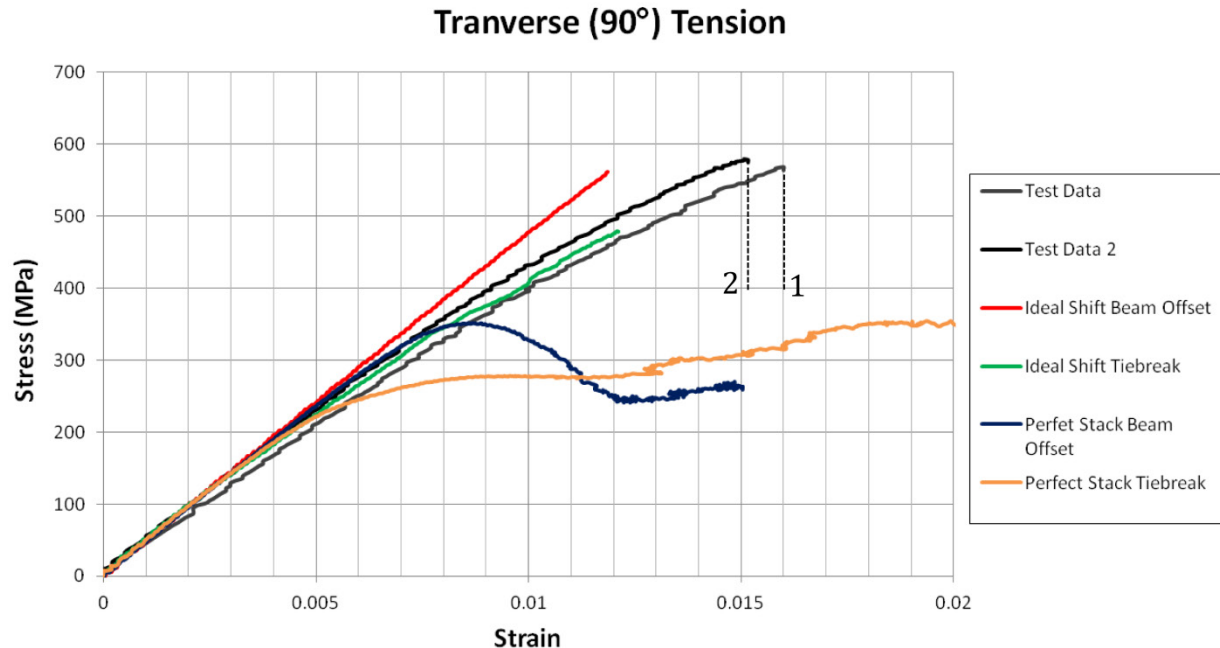
Tranverse (90°) Tension

Figure 27.—Stress-strain curves for the 90° coupon test for both contact types and stacking configurations. The experimental data is shown in gray and black and numbered on the figure. The colored lines represent the four simulation coupons with varying stacking or contact type as indicated in the figure legend.

between the two stacking configurations. For either contact definition, the perfectly stacked coupons showed premature material softening with final strengths well below the experimentally reported values. Similar to the 30° coupon, the ideally shifted coupon utilizing the beam offset contact best captured the final strength of the coupon. It should be noted, however, that the response with this configuration was linear elastic until failure. Both experimental stress-strain curves show a distinct nonlinearity after 0.5 percent strain which is not captured in the simulation results for the ideally shifted beam offset coupon. The possible source of this discrepancy is discussed later, along with the comparison of predicted failure modes.

Based on the previous results for all four simulated coupon types across the four testing directions, it was found that the ideally shifted coupon with the beam offset contact provided the best match to the overall composite behavior. This conclusion was based on comparisons between the experimental and simulated stress-strain curves and predicted strength values for the 30° and 90° coupons. The simulated results were relatively indifferent to stacking configuration for the other coupon directions. It should be noted again that the ideally shifted stacking configuration was a representation of the nesting of axial fibers during manufacture. The ideal shifting was a structured means of easily incorporating fiber nesting without dealing with a truly random through-thickness distribution. Thus, it can be only recommended over the perfectly aligned configuration, not generalized to be the best approach.

The beam offset contact type also provided the best match for the predicted braided coupon strengths. The tiebreak contact, which does not tie rotational degrees of freedom between shell layers, caused premature failure in the 30° and 90° coupons. One important item to note is the lack of predicted nonlinearity of the coupon response when using the beam offset contact for the 30° and 90° cases. This nonlinearity was observed experimentally in both cases. Nevertheless, it was deemed more relevant to capture the appropriate strength rather than the nonlinearity of the coupon response which may be more complex than the coarse subcell approach can capture.

Another important point to address from the simulations and the experimental work using DIC was the influence of contact type and shifting configuration on the simulation of the coupon directions which had the presence of free edge damage in the experimental tests. Figure 20 and Figure 22 show the presence of strain concentrations at the free edges of the 30° and 90° coupons, respectively. These two coupon directions are also the two simulated cases which do not load directly along a fiber tow path. Due to the sensitivity of these two coupon directions on contact type and/or stacking configuration, it is believed that these parameters (contact and stacking) play a role in load distribution and damage development when the coupon is not loaded in a fiber tow direction

Predicted Failure Modes

This section discusses the results of all off-axis coupon simulations using the aforementioned ideally shifted beam offset coupon for all cases. The experimental failure modes are compared with the FE model and the results are discussed. Similar to the previous study, the 45° coupon is omitted intentionally to provide final validation of the calibrated model.

The stress-strain curves for the 0° coupon are shown in Figure 28 for both the simulation case (ideally shifted with beam offset contact) and two experimental test cases. It should be noted that the experimental data was limited to the number of curves for which the DIC data was available (2 of 3). The observed nonlinearity of the simulation was a function of the MAT 58 exponential damage evolution. The simulation failure mode was a tensile failure of the axial plies, which corresponds well to the longitudinal failure of the axial tows from the experiment. The simulation failure occurred nearest to the grips due to the deterministic nature of the numerical solution, whereas the experiment failed both near the grips and at the gage section. The experimental curve which exhibits stiffening was a test which did not fail initially (due to insufficient grip displacement) and was subsequently reloaded. For more accurate comparison, the lower experimental test data should be used which matched well to the simulated response.

The stress-strain curves for the 30° coupon are shown in Figure 29. The two experimental coupons exhibited a range for the predicted strength (~450 and ~520 MPa). The simulated coupon (again, ideally shifted with beam offset contact) failed initially at 495 MPa, well within the two experimental data points. The predicted failure from the simulations was compressive failure of the bias tows oriented perpendicular to the load. A comparison between the experimental failure path and simulated failure modes is shown in Figure 30(a) and (b). The red elements shown in Figure 30(b) are elements whose bias plies have reached their longitudinal strength. The stresses in these plies were compressive. All other plies and ply directions remained intact in the simulation coupon, hence the simulated coupons were able to carry additional load after the initial failure (as shown by the post-peak response of the simulation in Figure 29). The experimental coupon did not show evidence of fiber tow failures aside from the compressive bias tow failures (axial tows and bias tows not perpendicular to the load were intact) and was relatively stiff compared to the other failed coupons. The stiffness and strength remaining in the simulation after the initial failure may be important in capturing the appropriate residual stiffness and strength of the composite post-impact and should not be dismissed. The termination of the experimental test was likely due to the significant load drop experienced during the compressive tow failure, resulting in a stop condition.
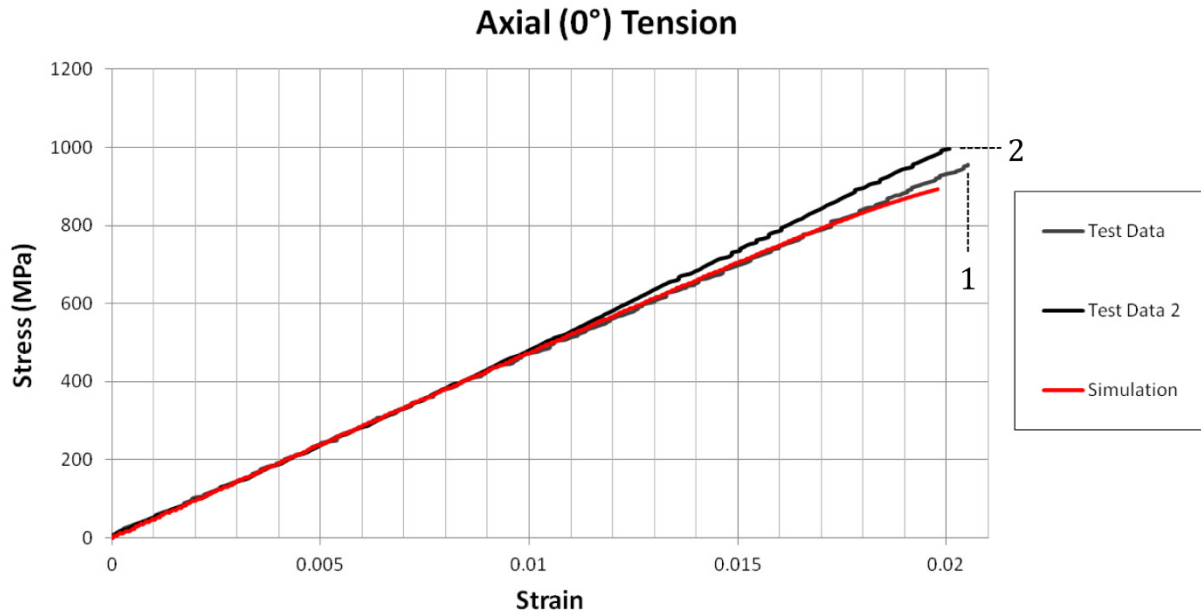
Axial (0°) Tension

Figure 28.—The stress-strain curve for the ideally shifted coupon with beam offsets in the 0° tensile test (red) along with two experimental stress-strain curves (black and gray, labeled).
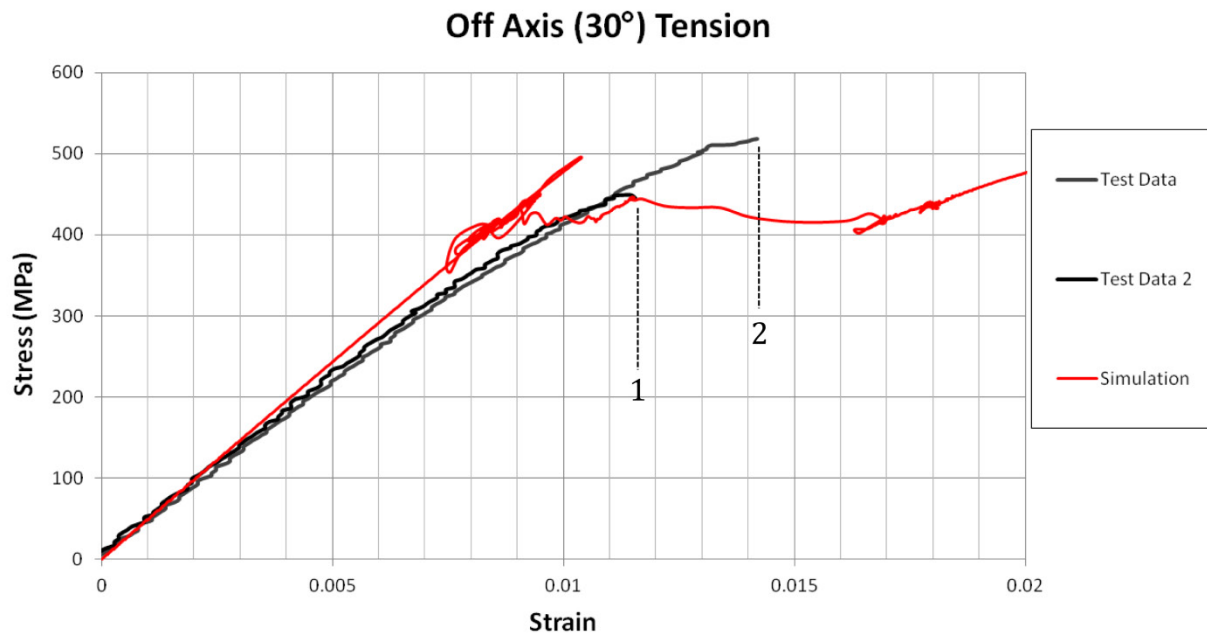
Off Axis (30°) Tension

Figure 29.—Stress-strain curve for the ideally shifted coupon with beam offsets in the 30° tensile test (red). Experimental data from two separate tests are included and labeled to identify the end point.

The simulation results in Figure 30(b) show a preferential alignment of the bias tow compressive failures along the 30° direction coincident with the axial fibers, which can also be observed in the experimental results in Figure 30(a). The simulation results, however, do not show localized failure along a single path, and damage progressed along two different axial tow paths as shown by the two long diagonal lines of red elements at the center of Figure 30(b). This diffuse damage development may be a limitation in the finite element discretization which is incapable of capturing discrete cracks. In the

current analysis, the failure surfaces of the UD plies are faceted, meaning the longitudinal, transverse and shear directions are uncoupled when determining the failure in the constitutive model. As such, the compressive longitudinal failure of the bias plies in the analysis does not necessarily cause tensile and/or shear failure in the same ply. This result was observed at various elements failed in the 30° simulated coupon. Since these ply layers were able to still carry load in the transverse and shear directions, they may have contributed to the development of additional compressive failures in the simulations outside of the origination of failure in the coupon. In the actual experimental test, the bias tows which fail in compression are completely severed and unable to carry transverse/shear load. The observed damage was highly localized. Aside from this difference, the model was able to correctly predict the coupon failure mode. In addition, the current analysis is deterministic. The introduction of probabilistic strengths or locally varying material properties (present in the real composite) may lead to more localized failures.

Figure 31 shows the stress-strain curves for the experimental and numerical coupons in the 60° coupon test for both the original simulation, which used the bias longitudinal strength obtained from the top down unit-cell approach, and the modified simulation which enforced a failure strain equivalent to the axial ply failure strain in the longitudinal direction. The modified simulation (with bias ply tensile failure strains set equal to the axial ply tensile strains) had a predicted strength of 830 MPa, correlating well with the reported experimental strengths of 828 and 862 MPa. These results are far improved from the original prediction of 464 MPa. In addition, this updated bias ply longitudinal strength did not affect the predicted strength or stress-strain response of the 0° and 30° coupon, since it was not a significant failure direction in those two directions.

Good correlation was found with the modified simulation results and the experimental data for the 60° coupon. One noted difference in the stress-strain curves is the apparent nonlinearity of the modified simulation at around 0.9 percent strain and is addressed here. This nonlinearity was caused by local plies

(a)
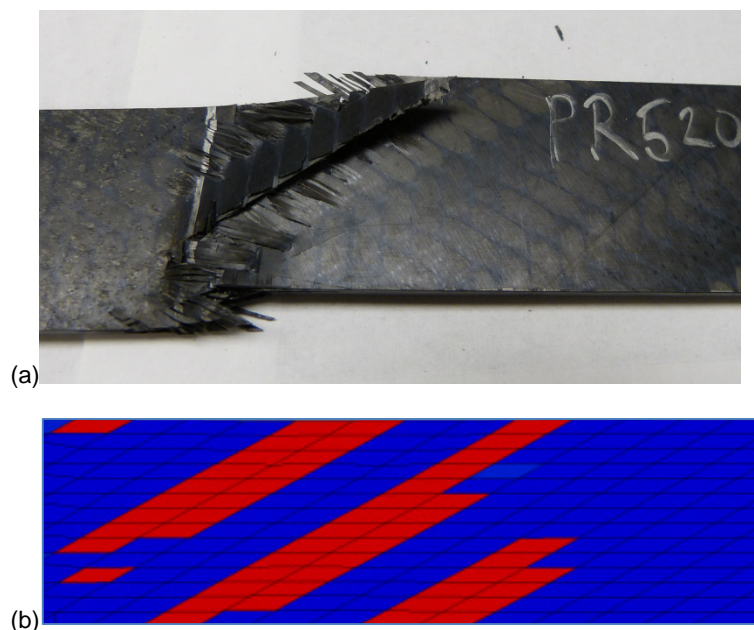

(b)

Figure 30.—(a) The experimental failure and (b) the predicted failure of the simulated 30° coupon. The color coding in figure (b) corresponds to red specifying an element whose integration point has reached the damaged state (D=1) in the longitudinal direction. The stress in these integration points (which corresponded to the bias tows lying perpendicular to the load) was compressive.
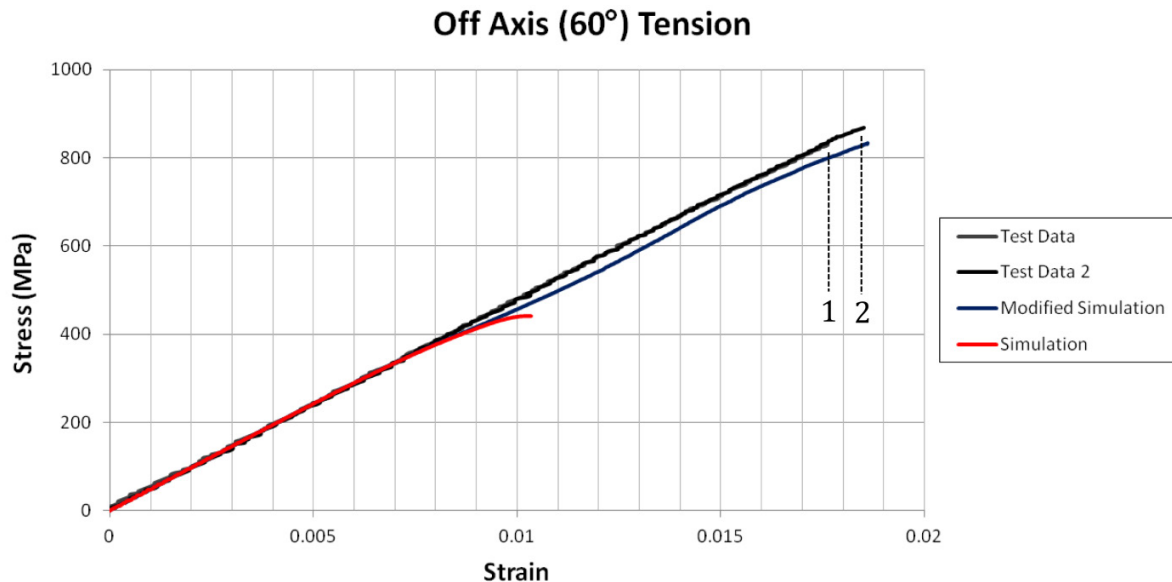
Off Axis (60°) Tension

Figure 31.—Stress-strain curves for the ideally shifted coupon with beam offsets in the 60° tensile test. Both the initial simulation (red) and the modified simulation (blue) which included the increased bias tow longitudinal tensile strengths are presented. Experimental data from two separate tests are shown (gray and black) with labels to distinguish the termination points.

(axial and bias) reaching their specified shear strength. Recalling from the sections on UD strength determination, the shear directions were modeled to have a plateau stress upon reaching their strength. This strength was reached in this case for the axial tow in shear, causing the softening of the coupon stiffness observed in Figure 31.

It is believed that the simulated nonlinearity in the numerical model was a result of the lack of continuity of bias tows in the subcell model. Due to the discretization of the model, axial tow continuity is preserved, while bias tow continuity is not. As a result, the load distribution in the 60° FE subcell model is carried disproportionately in shear by the axial and non-60° bias plies. The experimental coupon is loaded along the 60° bias tows which are continuous. The numerical coupon, on the other hand, does not load the bias plies directly, and instead has complex load transfers between adjacent A/B, B/C, C/D and D/A subcells.

The predicted failure mode of the composite for the 60° coupon was tensile failure of the bias UD plies in the longitudinal direction (direction of the applied loading). This correlates well with the experiment, as shown by the comparisons in Figure 32(a) and (b). As expected, the simulation results are highly localized to a small region near the grips of the coupon, due to the deterministic nature of the simulation. Additionally, the simulation is less catastrophic in terms of damage development; however, the extent of damage in the experimental test—as seen in Figure 32(a)—may be skewed by the post-failure pull out of bias tow fibers. In both the experiment and FE simulations, the tensile failure of the bias tows caused failure of the entire region, e.g., failure of all other material directions in the simulation.

The stress-strain curves for the 90° coupon are presented for both the simulation and experiments in Figure 33. Both the original simulation (which under-predicted the 60° coupon strength) and the modified simulation with updated bias ply tensile strains/strengths are presented. Although the original simulation predicted a strength value which matched well with the experimental data, the failure mode was a longitudinal failure of the bias tows. The experiment, on the other hand, was a function of edge-initiated shear failure, as shown by the image of the failed coupon in Figure 17 and the DIC strains prior to failure in Figure 22. As a result, the increased bias tow tensile strength in the modified simulation causes an over-estimation of the composite strength in the 90° direction. The over prediction may be due to limitations of the current model which is not sufficient to represent the free-edge effects in the 90° coupon.

(a)

(b)
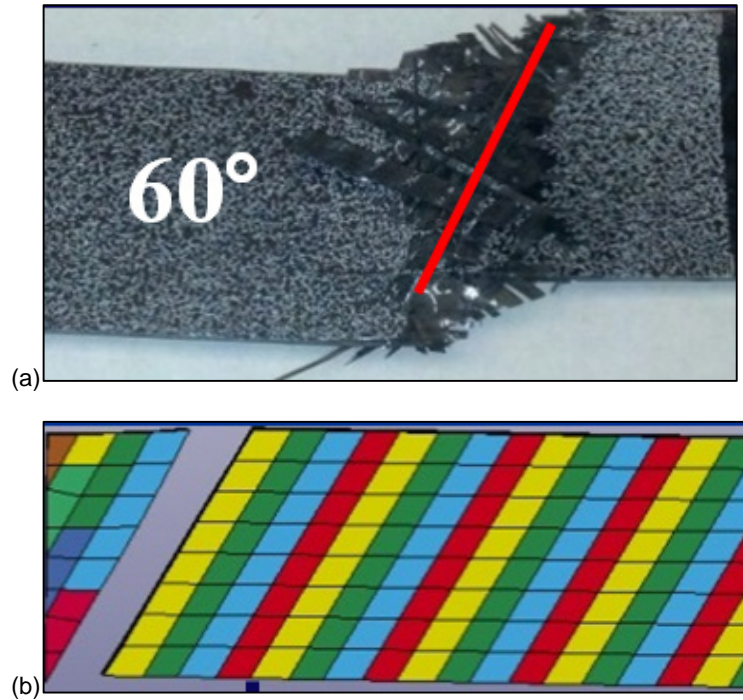
Figure 32.—(a) The experimental failure and (b) the predicted failure of the simulated 60° coupon. In (b), the colors correspond to different subcell regions, and not to damage values as in previous plots.

Figure 33.—Stress-strain curves for the ideally shifted coupon with beam offsets in the 90° tensile test. Both the initial simulation (red) and the modified simulation (blue) which included the increased bias tow longitudinal tensile strengths are presented. Experimental data from two separate tests are shown and labeled

Figure 34 overlaps the DIC images captured during experiment with the stress-strain curves obtained by simulation and experimental measurement. The figure illustrates the development of surface cracki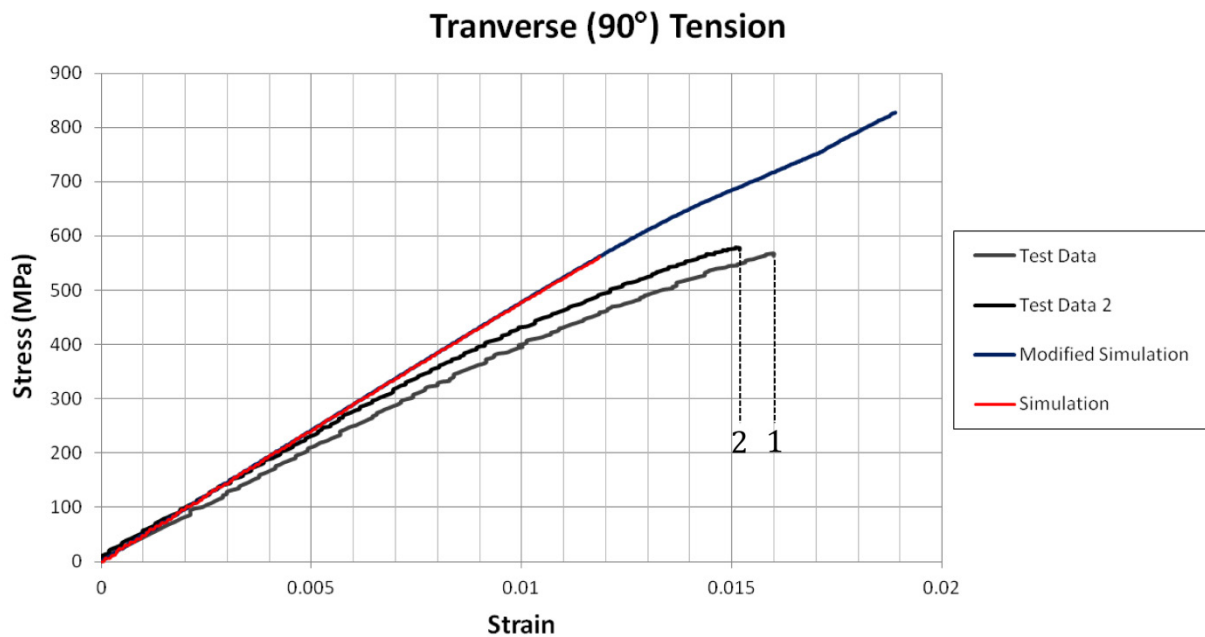ng and the out-of-plane displacements at the free-edges. This localized damage is believed to be one of the sources of material nonlinearity in the overall coupon response. An additional source of coupon nonlinearity is also believed to be fiber straightening within the matrix, due to the unrestrained fiber tows at the edges. These complex mechanisms are not captured by the current subcell model, which may be a limitation of the current level of fidelity in the model. For example, Kohlman (2012) observed tow shearing (between axial and bias tows at the free edge) as a predominant failure mechanism based on coupon observations. Any method attempting to capture these mechanisms explicitly, however, will incur significant computational cost.

On the other hand, it is worth mentioning that these free-edge effects are typically mitigated in the design of composite structures and are less critical in the determination of failure in flat panel impact tests or other realistic structural scenarios. In a real composite structure, the ideal case 90° failure due to longitudinal failure of the bias tows, which is simulated in the present subcell model, may be the actual failure mode when the material is utilized in a realistic large scale structure. Thus, the inability of the subcell model to capture the 90° failure mode and failure strength observed in the straight sided coupon is not a critical flaw to the approach's usefulness as a modeling tool.

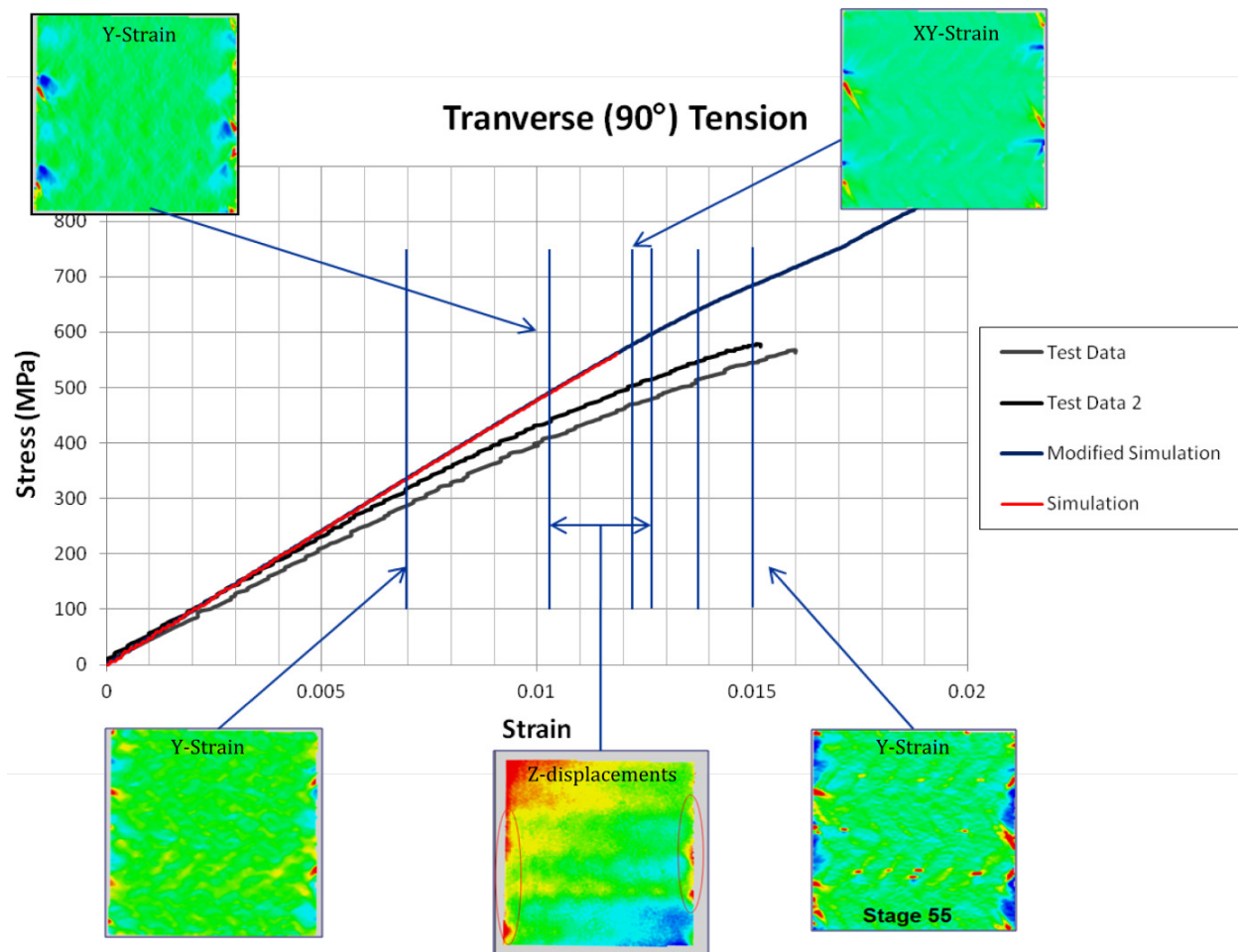Figure 34.—Stress-strain curves for the simulation and experiment overlapped with DIC images of both the shear and longitudinal strains (w.r.t. the loading direction) at various points along the experimental curve. The vertical lines represent the onset of the observed localized strains or displacements in the experimental test. X-strain and y-strain components correspond to the axial and transverse directions, respectively.
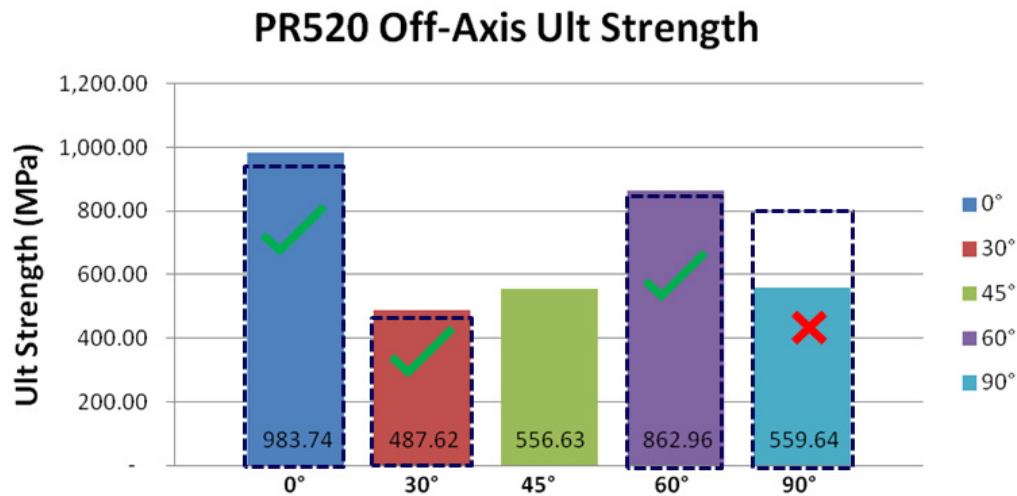
Figure 35.—Comparison between the reported strength values and the modified simulation response (dashed boxes). The green check marks correspond to simulations where the failure mode in the simulation matched the observed experimental failures. The red X corresponds to a difference in failure mode predictions in the 90° coupon.

Additionally, previous works have shown the transverse (90°) strength of triaxially braided composites to be significantly higher without the edge effect. Salem et al. (2014) performed burst tube tests to help characterize the transverse, or 90°, strength of the coupon without the influence of free edges. The composite tubes were made of T700 fiber tows, the Epikote 862 (E862) resin and an identical braiding architecture to the system in the current work. They were pressurized internally to cause a uniform loading in the hoop stress direction, which can be idealized as a transverse load for a standard coupon. The authors reported a more than 50 percent greater value of the final failure strength over those reported from straight sided coupon tests. The reported failure strain value was in the range of 1.5 to 1.9 percent. These observations can be compared qualitatively to the trends observed in the modified simulation of the 90° coupon shown in Figure 33. In the subcell simulation of the T700/PR520 90° coupon, the 44 percent over prediction of the straight sided coupon strength and predicted 1.9 percent failure strain may suggest the subcell model exhibited an appropriate material response if free edge effects are neglected.

A summary of the predicted strengths in the modified subcell model are shown in Figure 35. The results indicate that the subcell model performed well in predicting the failure mode and experimental strength for three of the four tests cases. The response of the 90° coupon which was susceptible to edge damage and hence was not captured appropriately by the FE model.

Conclusions

A combined experimental and analytical approach has been presented to verify the proposed subcell modeling approach in capturing the behavior of 2D triaxially braided composites. The proposed modeling approach combined top down coupon level strength data with computational micromechanics to obtain model parameters.

To provide coupon level data, tensile experiments were carried using straight sided braided composite coupons loaded at five orientations. DIC was used to monitor the damage initiation and failure process during tensile tests. The experimental results showed that the failure strengths and failure modes of the

straight sided coupons of the braided composites were sensitive to the loading configuration. Coupons with five different orientations displayed a range of failure modes and strengths despite the intended quasi-isotropic nature of the braid design. The 0° and 60° directions had the highest failure strengths, whereas the 30°, 45° and 90° coupons had significantly lower reported strengths. The latter three coupon tests were susceptible to edge cracking and possible edge initiated damage.

A study of two different stacking configurations (through the thickness of the braid) and two different contact types assisted in identifying the most appropriate combination to accurately capture the braided coupon response. A strong contact between individual shell layers, which tied rotational and translational degrees of freedom, was found to best predict the experimental strengths. In addition, the best correlation to the experimental data was obtained for all directions when using a shifted coupon model which accounts for the nesting of axial tows observed in manufactured composites.

The subcell model was successful in predicting the failure modes and coupon strengths for the 0°, 30° and 60° coupons. A discrepancy in the original characterization of the bias tow longitudinal tensile strength was identified. The top-down methodology was modified and alternative assumptions were provided. The modified simulations provided an improved fit to the experimental data.

The predicted strength of the 90° coupon test was much higher in the simulations. In addition, the predicted failure mode did not match to those observed from the experiments. The experimental failure modes were known to be caused by damage initiated at the free edge. The experimental DIC strain data show significant localization of strains at the free edge which is not captured in the simulation. In addition, a lack of an intra-tow interface in the subcell method limits the current approach in simulating these failure modes. The simulated response, however, matches qualitatively with the strength determined by the tube burst tests with a similar composite system, indicating that the subcell modeling approach would appropriately capture the appropriate 90° coupon strength in the absence of the free edges.

The result indicates that the free edge effect can significantly reduce the strength of braided composites at certain orientations. Therefore, the design and manufacturing strategies which reduce or eliminate the exposure of free edge for these orientations should lead to a significant improvement of the load bearing capability and the integrity of the structure.

In summary, the subcell approach shows promise in providing an improved analysis capability for braided composite structures with high computational efficiency. In the next phase, this approach along with the best practices reported here will be validated in the simulation of 45° coupon under tension and panel impact experiments.

Appendix

This section contains the significant LS-DYNA keywords used for the current subcell modeling work. These include the keywords used to define the subcell stacking (*Section_Shell), the integration rules for the subcells (*Integration_Shell), the contact keyword for the beam offset type contact and the material card. Additional information on the exact input should be referenced to the LS-DYNA user's manual (Hallquist 2006).

Figure A.1 shows the section definition used to define subcell A. The information contained within the card includes the shell thickness, element type, integration rule, and stacking orientation of the UD plies. Figure A.2 contains the associated integration rule card referenced by the *Section_Shell keyword of subcell A. The *Integration_Shell keyword contains the location, thickness and associated material specifier for each layer of the composite shell (subcell). Figure A.3 presents the keyword for the use of MAT58 (*Mat_Laminated_Composite_Fabric) for the axial ply (V_f = 80 percent). Lastly, Figure A.4 provides an example of the contact keyword used to define the beam offset type contact.

```
*SECTION_SHELL
$...>....1....>....2....>....3....>....4....>....5....>....6....>....7....>.
$Sub-cell A
$#    secid    elform      shrf       nip     propt    qr/irid     icomp     setyp
          2         2  1.000000         3         1         -2         1         1
$#       t1        t2        t3        t4      nloc     marea      idof    edgset
 2.0830E-2 2.0830E-2 2.0830E-2 2.0830E-2     0.000     0.000     0.000         0
$#       bi        bi        bi        bi        bi        bi        bi        bi
-60.000000     0.000 60.000000     0.000     0.000     0.000     0.000     0.000
```

Figure A.1.—The *Section_Shell keyword for Subcell A. This keyword contains the definition of the element type, shell thickness and the orientation of the unidirectional plies. (Units are in inches.)

```
*INTEGRATION_SHELL
$#     irid            nip      esop    failopt
          2              3         0          0
$#        s             wf       pid
 -0.745380       0.254620         3
     0.000       0.490760         1
  0.745380       0.254620         3
```

Figure A.2.—The *Integration_Shell keyword for subcells A and C. Contained in the keyword are the thicknesses of each unidirectional lamina within the subcell, the location of the integration point and the associated material specifier for the layer.

```
*MAT_LAMINATED_COMPOSITE_FABRIC
$        MID          RO          EA          EB         (EC)        PRBA        TAU1      GAMMA1
$#       mid          ro          ea          eb         (ec)        prba        tau1      gamma1
          1  1.6900E-4  2.6803E+7  1.6534E+6  1.6534E+6  1.5240E-2  7251.8901  4.5400E-3
$        GAB          GBC         GCA      SLIMT1      SLIMC1      SLIMT2      SLIMC2       SLIMS
$#       gab          gbc         gca      slimt1      slimc1      slimt2      slimc2       slims
  9.1230E+5  5.0700E+5  1.6244E+6  1.0000E-2   0.100000    1.000000    1.000000    1.000000
$       AOPT        TSIZE       ERODS        SOFT          FS
$#      aopt        tsize       erods        soft          fs
   3.000000       0.000    0.300000       0.000  -1.000000
$                                            A1          A2          A3
$#        xp           yp          zp          a1          a2          a3
    0.000        0.000       0.000       0.000       0.000       0.000
$                                            D1          D2          D3        Beta
$#        v1           v2          v3          d1          d2          d3        beta
   1.000000       0.000       0.000       0.000       0.000       0.000   60.000000
$       E11C         E11T        E22C        E22T         GMS
$#      e11c         e11t        e22c        e22t         gms
  7.4620E-3  1.9470E-2  1.7100E-2  1.2313E-2  6.6000E-2
$         XC           XT          YC          YT          SC
$#        xc           xt          yc          yt          sc
  2.0000E+5  5.2200E+5  28398.391  21719.400  28398.391
```

Figure A.3.—The *Mat_Laminated_Composite_Fabric keyword for the axial unidirectional ply (V_f = 80 percent). Moduli and strength values are listed in units of psi.

```
*CONTACT_TIED_SHELL_EDGE_TO_SURFACE_BEAM_OFFSET
$#     ssid         msid       sstyp       mstyp      sboxid      mboxid         spr         mpr
          4            1           4           0           0           0           1           1
$#       fs           fd          dc          vc         vdc      penchk          bt          dt
   0.300000    0.280000       0.000       0.000   20.000000           1      0.0001 1.0000E+20
$#      sfs          sfm         sst         mst        sfst        sfmt         fsf         vsf
   1.000000    1.000000       0.000       0.000    1.000000    1.000000    1.000000    1.000000
$#     soft       sofscl      lcidab      maxpar       sbopt       depth       bsort      frcfrq
          1        0.000           0       0.000       0.000           0           0           0
```

Figure A.4.—The contact keyword used to define contact between the shell element layers. The slave surface for the contact was prescribed using node sets while the master surfaces were specified through the use of segments.

References

Aboudi, J., Arnold, S. M., and Bednarcyk, B. A. (2012). "Micromechanics of Composite Materials: A Generalized Multiscale Analysis Approach." Butterworth-Heinemann, Oxford, UK.

Ayranci, C. and Carey, J. (2008) "2D braided composites: A review for stiffness critical applications." *Compos. Struct*, 85:43–58.

Bednarcyk, B. A. and Arnold, S. M. (2002). "MAC/GMC 4.0 User's Manual—Keywords Manual." NASA Technical Memorandum, NASA/TM—2002-212077/VOL2.

Blinzler, B. J. (2012). "Systematic Approach to Simulating Impact for Triaxially Braided Composites." Ph.D. thesis, University of Akron, Akron, OH.

Cater, C., Xiao, X., Goldberg, R.K., W. Kohlman, L.W. (2014). "Single and Multi-ply Braided Composite Response Predictions using Modified Subcell Approach." *J Aerosp Eng*, 04014117, 1-12.

Cheng, J., and Binienda, W. (2008). "Simplified Braiding through Integration Points Model for Triaxially Braided Composites." *J Aerosp Eng*, 21, 152–161.

Goldberg, R. K., Blinzler, B. J., and Binienda, W. K. (2010). "Modification of a Macromechanical Finite Element Based Model for Impact Analysis of Triaxially Braided Composites." *J Aerosp Eng*, 25, 383-394.

Hallquist, J. Q. (2006). "LS-DYNA® Keyword User's Manual." Volume II Material Models, Version 971, Livermore Software Technology Company, Livermore, CA.

Kohlman, L. W. (2012). "Evaluation of Test Methods for Triaxial Braid Composites and the Development of a Large Multiaxial Test Frame for Validation Using Braided Tube Specimens." Ph.D. thesis, University of Akron, Akron, OH.

Li, X., Binienda, W. K., and Littell, J. D. (2009). "Methodology for Impact Modeling of Triaxial Braided Composites Using Shell Elements." *J Aerosp Eng*, 22, 310–317.

Littell, J. (2008). "The Experimental and Analytical Characterization of the Macromechanical Response for Triaxial Braided Composite Materials." Ph. D. thesis, University of Akron, Akron, OH.

Liu, K., Chattopadhyay, A., Bednarcyk, B., and Arnold, S. (2011), "Efficient Multiscale Modeling Framework for Triaxially Braided Composites using Generalized Method of Cells," J. Aerosp. Eng., 24, 162–169.

Matzenmiller, A., Lubliner, J., and Taylor, R. L. (1995). "A Constitutive Model for Anisotropic Damage in Fiber Composites." *Mech Mater*, 20, 125-152.

Quek, S. C., Waas, A. M., Shahwan, K. W., and Agaram, V. (2006). "Failure mechanics of triaxially braided carbon composites under combined bending-compression loading." *Compos Sci Technol*, 66, 2548–2556.

Quek, S. C., Waas, A., Shahwan, K. W., and Agaram, V. (2004). "Compressive response and failure of braided textile composites: Part 2—computations." *Int J Nonlinear Mech*, 39, 649–663.

Roberts, G. D., Goldberg, R. K., Binienda, W. K., Arnold, W. A., Littell, J. D., and Kohlman, L. W. (2009). "Characterization of triaxial braided composite material properties for impact simulation." American Helicopter Society. Grapevine, TX, USA. 2507–2528.

Salem, J.A., Bail, J.L., Wilmoth, N.G., Ghosn, L.J, Kohlman, L.W., Roberts, G.D., Martin, R.E. (2014). "Burst Testing of Triaxially Braided Composite Tubes." NASA/TM—2014-216615

Schweizerhof, K., Weimar, K., Munz, Th., and Rottner, Th. (1998). "Crashworthiness Analysis with Enhanced Composite Material Models in LS-DYNA—Merits and Limits." 5th International LS-DYNA User's Conference, Southfield MI.

Song, S., Waas, A. M., Shahwan, K. W., Xiao, X., and Faruque, O. (2007). "Braided textile composites under compressive loads: Modeling the response, strength and degradation." *Compos Sci Technol*, 67, 3059–3070.

van der Sluis, O., Schreurs, P.J.G., Brekelmans, W.A.M. and Meijer, H.E.H. (2000). "Overall behaviour of heterogeneous elastoviscoplastic materials: effect of microstructural modeling." *Mech Mater*, 32, 449-462.

Xiao, X., Kia, H. G., and Gong, X.-J. (2011). "Strength prediction of a triaxially braided composite." *Compos Part A*, 42, 1000–1006.

Yuan, Z., and Fish, J. (2008). "Toward realization of computational homogenization in practice." *Int J Numer Meth Eng*, vol. 73, Jan. 2008, pp. 361–380.

Zhang, C., Binienda, W. K., and Kohlman, L. W. (2013). "Analytical and Numerical Analysis on Elastic Behavior of Triaxial Braided Composites." *J Aerosp Eng*, 2013, 10.1061/(ASCE)AS.1943-5525.0000369.

Zhang, C., Binienda, W. K., Goldberg, R. K., and Kohlman, L. W. (2014). "Meso-scale failure modeling of single layer triaxial braided composite using finite element method." *Compos Part A*, 58, 36–46.